THE EFFECTS OF FLUID FLOW ON SHEAR LOCALIZATION AND FRICTIONAL STRENGTH FROM DYNAMIC MODELS OF FAULT GOUGE DURING EARTHQUAKES

A Thesis

by

RONALD LOUIS BIANCO

Submitted to the Office of Graduate and Professional Studies of
Texas A&M University
in partial fulfillment of the requirements for the degree of

MASTER OF SCIENCE

Chair of Committee,	David W. Sparks
Committee Members,	Benchun Duan
	Marcelo Sanchez
Head of Department,	John R. Giardino

December 2013

Major Subject: Geophysics

ABSTRACT

This thesis explores the effects of fluid flow on shear localization and frictional strength of fault gouge through the use of a coupled 2-phase (pore fluid-grain) Finite Difference-Discrete Element Numerical model. The model simulates slip at earthquake velocities (~$1^{m}/_{s}$) in a fluid saturated gouge-filled fault. We find three types of shear behavior: (I) distributed shear, (II) random internal localization, and (III) boundary localization. Each shear type is dependent on the applied shear velocity, V, effective confining stress, N, and internal permeability, k. Through quantitative analysis of the positions and magnitude of localized shear bands, we show under which conditions the presence of and transitions between these shear types will occur. During shear, fluid pressure deviations, ΔP, are generated by dilation and compaction cycles. The fluid effects on the system are more pronounced in simulations with higher V and lower N and k. Relative to the dry experiments, fluid saturated systems have an increased localization toward the boundaries of the gouge layer (type III), and no occurrence of distributed (type I) shear.

Systems with lower N and k show liquefaction events. Liquefaction events originate from increases in fluid pressure, ΔP, around force chains between grains. Once $\Delta P \approx N$, the high pressures weaken the frictional forces between grains and destroy force chains. Shear then occurs at essentially zero friction until a new grain configuration recreates force chains. A reduction in mean friction is seen for systems with large liquefaction events (without inclusion of thermal pressurization), which could

introduce a new mechanism in low friction faults. We also find that systems undergoing different types of shear will all trend toward type (III) shear following a liquefaction event.

TABLE OF CONTENTS

Page

LIST OF FIGURES

LIST OF TABLES

TABLE Page

1. INTRODUCTION

Earthquakes are generated by the release of kinetic energy stored in the country rock during frictional sliding which takes place along a fault plane. The movement of the country rock in the faults can either be continuous (stable creep), or it can have a stick-slip (unstable) movement that will generate earthquakes.

As fault blocks move along each other's surfaces, surface asperities that can no longer take the applied stresses will break away from the country rock creating a granular medium located between the two faulted sections of rock. The development of this gouge layer and the forces governing the deformation of the granular medium under constant shear has been extensively studied through deformation experiments conducted in controlled environments (Mair and Hazzard 2007, Marone et al., 1990, Beeler and Tullis, 1996), and along outcrop evaluations (Cain et al., 1996, Chester, 1982). Field evidence (Chester and Lorgan, 1987) and numerical models (Ciamarra et al., 2012) show that the majority of shearing that takes place in a fault zone is concentrated along the fault gouge layer. Seismic energy released during large earthquakes is also directly linked to the generation of tsunamis, and are suggested to initiate large fluxes of fluid through fault zones through the process of "fault valving" (Sibson, 1990).

The granular gouge zones of most fault zones will be saturated with fluids, which can play an important role in the dynamics of the fault. For example, aftershock patterns from the 1997 Colfiorito earthquake have been interpreted as being triggered by a high-pressure fluid migrating up the fault plane from depth (Mitchell and Faulkner, 2008).

Fluids have also been suggested to be responsible for seismic tremor or "slow" earthquakes (Robin et al., 1979, Sleep and Blanpied, 1992).

The fluids within the gouge flow in and out of the layer either along the fault plane or through fractures in the surrounding rocks. Faults and fractures in brittle rock are formed through the communication of many smaller tensile cracks as demonstrated from experiments and models (D.A. Lockner 1998, Healy and Holdsworth, 2006). As differential stress is applied to intact rocks, the amount of microfracture damage will accumulate as the rock approaches failure, and the resulting dilatancy will directly affect both porosity and permeability (Ebrahimian et al., 2011, Miller and Nur, 2000). Compaction along fault zones increases fluid pressure that can induce dilatants slip events which increase local permeability. The high pressures are then equilibrated into neighboring pore spaces, followed by a reduction in permeability through healing and sealing. The continued slip along preexisting fault surfaces will also generate cumulative damage into the country rock (Chester and Chester, 2000), where the microfracture damage surrounding the fault zone will vary significantly having a direct effect on the permeability of the surrounding rocks

The laws governing granular fault gouge stability with the inclusion of pore fluids are still largely unknown. This is due to the still explored dynamic properties exhibited by a solid matrix of grains undergoing shear. It is important that we understand the nature of the transient stability of fault gouge behavior and their roles that this instability plays in earthquake generation, along with the fluid flow transport properties controlled by rocks and fault heterogeneities.

1.1 FLUIDS AND PORE PRESSURE

Fluids in the pore spaces of a shearing gouge layer can drastically change the overall stability of the system, whether the motion is continuous or stick-slip due to repeated cycles of compaction and dilation (El Shamy and Zeghal 2007, Goren et al., 2010, R. Iverson, 1993). During earthquakes, a sheared granular matrix will experience both compaction and dilation, which cause multiple increases and decreases in pore pressure. An increase in pore pressure can lower the systems resistance to shearing by offsetting the normal stresses, and in extreme cases, where pressure exceeds lithostatic, the granular matrix will behave as a liquid instead of a solid, leading to liquefaction (Okada and Ochiai 2007, Rozhko et al., 2007). Alternatively, a drop in pressure can strengthen (harden) the system by increasing the effective normal stress on grain contacts, and increasing the frictional forces (Scholtz et al., 1973).

The effects of fluid within country rock can also be seen in the after effects of earthquakes as the rocks try to relax into a state of equilibrium. After an earthquake has increased or decreased pressure in the gouge zone of a fault, this pressure will equilibrate with the surrounding country rock over some time period. This drives fluid flow that changes the pressure conditions along the entire fault zone and surrounding faults, and can lead to visco-elastic relaxation of the country rock. Satellite radar interferograms for two large (6.5 magnitude) earthquakes in Iceland showed that deformations recorded within the first couple of months following the events could not be caused by stable slip or visco-elastic rebound, but rather the data points to deformation caused by porous elastic rebound (Jónsson et al., 2003). This finding gives us another example that the role

of fluid flow at depth during these events can be a large controlling factor within a seismically altered rock body.

It has been documented that in a two-phase system (matrix of elastic grains, connected network of viscous fluid) that the shear stress needed to shear the system, τ, is a function of the effective normal stress (K. Terzaghi, 1943):

$$\tau = \mu(\sigma_n - P) \quad (1)$$

where μ is a friction coefficient, σ_n is the total normal stress across the fault, and P is pressure. As P increases toward σ_n the system will lose its shear strength, and if P decreases the system becomes more resistant to shear showing the importance that the pore pressure has on the overall stability of the system.

Goren et al. (2010) described a dimensionless Deborah number (De) that acts as a controlling factor in the evolution of pressure in a deforming granular layer. This number is the ratio of the time scale for pressure equilibration by fluid flow to the time scale for pressure generation by dilation and compaction of pore space during grain rearrangements. De depends on properties of the grain and fluid (e.g. permeability, viscosity, compressibility) and characteristics of the deformation (strain rate). When De>> 1, the distance from a region of porosity change to a region of unchanged pressure is very large so that fluid flow is ineffective. This could occur either in a very large granular layer with low permeability, or a layer with undrained (no flow) boundaries. In this system, fluid mass in the gouge is conserved, so all of the compaction and dilation are translated into changes in pressure. The pore pressure now depends on the fluid compressibility, β, and the pressure is proportional to strain (measured relative to some

initial state). In this scenario it has been shown (Goren et al, 2010, Samuelson et al, 2009, Segall et al, 2010) that the evolution of pore pressure comes from the relationship between the pressurization and depressurization of the system. As the system dilates from its original dense packing, the pore pressure decreases, causing an increase in the friction between grain contacts resulting in system hardening. Alternately, during compaction the elastic behavior will cause the pore pressure to rise rapidly until it becomes equal to the normal effective stress causing rapid liquefaction and a loss of shear resistance (Goren et al. 2011).

If both the gouge layer and the surrounding rock are highly permeable, then De << 1. In these instantly drained systems pressure diffusion is very rapid, so there is no change seen in the pressures throughout the system during compaction or dilation events. Here there is no difference between dry or fluid saturated simulations, as the pressure can instantly drain out of the system; therefore, changes in the system shear behavior are reliant on variations in the effective confining stress.

When De is of the order 0.1 to 10, the system is drained (boundaries allow fluid flow), but not instantly, so that out-of-equilibrium pressures develop in the gouge layer. In experiments with open boundaries but moderately low gouge permeability (~10^{-14} m^2), Goren et al. (2010) observed that when dilation starts the pore pressure will first drop to a negative value and will then return toward a zero value due to the influx of fluid from the boundary. When $(De \sim 1)$ the pressures generated are approximately proportional to the strain rate, and the system has a viscous-like rheology.

The drained boundary condition (fixed P outside of granular layer) is equivalent to having an infinite reservoir of fluid outside the boundary with an infinite permeability. Due to the ease with which fluid is able to be supplied and taken away from the granular layer in this case, the boundary condition overstates the ability of the system to drain (Samuelson et al, 2009). Therefore, a natural gouge layer bounded by rock that has its own permeability and the combination of flow in the gouge and in the rock will determine the drainage.

It has been shown that country rocks with low permeability can act as barriers around the fault gouge trapping fluids within it causing pore pressures to rise above hydrostatic pressures and can commonly approach those of lithostatic (J. Byerlee 1990, Mitchell and Faulkner, 2012). The fluids within the gouge layer are allowed to permeate in and out of the layer either along the fault plane or through fractures in the surrounding rocks. Faults and fractures in brittle rock are formed through the communication of many smaller tensile cracks as demonstrated from experiments and models (D.A. Lockner 1998, Healy and Holdsworth 2006). As differential stress is applied to intact rocks, the amount of microfracture damage will accumulate as the rock approaches failure, and the resulting dilatancy will directly affect both porosity and permeability (Mitchell and Falkner, 2008). The continued slip along preexisting fault surfaces will also generate cumulative damage into the country rock (Chester and Chester, 2000), where the microfracture damage surrounding the fault zone will vary significantly having a direct effect on the permeability of the surrounding rocks (Mitchel and Falkner, 2008). It is constraints of the country rock along the gouge layer boundaries such as this

that drives the generation of our research, which can then be used to obtain a detailed investigation into the limiting factors on permeability and the spatial and temporal evolution of fault gouge dynamics.

1.2 MODELS OF FAULT DYNAMICS

The role that the evolution of the pore pressures within the gouge layer plays in fault stability is still unknown as it is impossible to conduct an experiment on a realistic fault scale. Due to this uncertainty, the gouge layer is not included in a large number of the models that are used to study theoretical faults and to represent paleo-faults as they try to gain an insight on the forces driving these fault's movements. Since slip along a fault zone occurs within the gouge layer, models that do not include the presence of the gouge layer must make limiting assumptions within the model by defining quantities for certain parameters including: porosity, permeability, contact friction, and pressures (Segal and Rice, 1995, T. Yamashita, 1999).

Discrete Element Method (DEM) numerical models are used to investigate the mechanical behavior of granular media at the individual grain scale. DEM models of granular material use assemblies of either 2D disks or 3D spheres. The conventional DEM formulates the interaction between two grains through contact spring forces and damping forces in both the normal and tangential directions (Cundall and Strack 1979). Many other works use DEM modeling of dry gouge layers to explore the dynamic interactions between grains under shear, such as: the effects of porosity and shear strength (Antonellini and Pollard 1994, Mair and Hazzard 2007, Makedonska et al., 2011, Place and Mora 1999), frictional rolling vs. sliding under different effective stress

(Aharonov and Sparks 2002), the effects of granular sphericity and roughness on shear zone localization (Kock and Huhn 2007, Morgan and Boettcher 1999), and fault gouge generation through cohesive grain bonding (Mair and Abe 2011) and evolution (Marone et al., 1990).

Due to the complexity of modeling fault stability, many studies use continuous shear to explore the dynamic behavior of gouge material (Jiang et al., 2010, Segal et al., 2010). Numerical studies of shearing granular layers have established that the behavior of the gouge layer is typically controlled by both the applied shear velocity, *V*, and the applied confining stress, *N* (Ausilio et al. 2008, P. Guo, 2012, Hadizadeh et al., 2010, Wong and Band, 2012). If we approach the granular behavior as particle flow under constant shear, then we can describe this flow using the so-called Inertia Number (Shojaaee et al. 2012):

$$I = \dot{\gamma}\sqrt{\frac{m}{N}}$$

Here, I is a function of the shear rate $\dot{\gamma}$, m is the mass of a grain, and, N, is the normal stress on the system. Shojaaee et al., 2012, shows that shear within dry granular systems will exhibit different trends for granular systems with different values of I. They also show that shear localization is effected by the roughness of the wall boundaries. Systems with rough boundaries will show more localized shear, whereas smooth walls will exhibit more localized shearing towards the boundaries.

Previous works (Goren et al., 2010 and Shojaaee et al., 2012) have given new insights into the complexity of shearing behavior in granular material. However, little is still known about the relationships between compaction, dilation, pressure, and shear

localization in fluid saturated gouge material. We use a Discrete Element Method numerical model of a fluid filled fault gouge to obtain new understanding of the effects of evolving porosity and permeability on deforming granular layers. In order to study the effects of these fluids, we will use the Goren et al. (2011) model of a two-phase system modified from the DEM model of Aharonov and Sparks (1999). In addition, this work adds the effect of fluid flow and pressure equilibration within a variable permeability damage zone surrounding the fault.

2. DISCRETE ELEMENT MODEL OF A GRANULAR MATERIAL

The Aharonov and Sparks numerical model used to study the evolution of pore pressures on a granular matrix maps the interaction of granular particles as a transient problem set forth by Cundall and Strack (1979) calculating the resulting forces on any sphere that is in contact with another at all times. To calculate the forces between grains, we use the force-displacement law as defined by Aharonov and Sparks 1999, to measure the forces between two grains that are in contact with each other based on the distance between the centers of the two grains, r_{ij}. If r_{ij} is less than the sum of the two grains' radii, $R_i + R_j$, the grains are in contact. The repulsive contact force depends on the amount of overlap between grains *i* and *j* given by: $\xi_{ij} = R_i + R_j - r_{ij}$.

The contacts have a normal (F^n) and shear force (F^s) associated with them. We can evaluate these forces with the Hertz-Mindlin contact model. The normal force on the contact is given by:

$$F_{ij}^n(t) = \left[\tilde{k}_n \xi_{ij} - \gamma m_{ij}\left(\dot{\boldsymbol{r}}_{\boldsymbol{ij}} \cdot \boldsymbol{n}_{\boldsymbol{ij}}\right)\right]\hat{n}_{ij} \tag{2}$$

where the first term is a nonlinear elastic repulsive force, and the second is a dampening viscous force where $\dot{r}_{ij}$ is the relative grain velocity, and $\hat{n}_{ij}$ is the unit vector normal to the contact (Goren et al., 2010). In the first term of eq. (2) we set the coefficient of the normal repulsive force to the nonlinear normal stiffness:

$$\tilde{k}_n = \frac{\sqrt{2}E}{3(1-\nu^2)}\left(R_{ij}\xi_{ij}\right)^{1/2} \tag{3}$$

Here E is the grains bulk modulus, ν is Poisson's ratio, and R_{ij} is the harmonic mean of the grains radii (Goren et al., 2010). The calculation of the contact shear force uses an elastic frictional law:

$$F_{ij}^{s}(t) = -\left[\min\left(\tilde{k}_s \;\; s, \mu F_{ij}^{n}\right)\right]\hat{s}_{ij} \tag{4}$$

Here s is shear displacement relative to the origination of the contact, μ is the surface friction coefficient, and $\hat{s}_{ij}$ is the unit vector tangent to the contact. Similarly to eq. (3), the coefficient in the tangent repulsive force is given by:

$$\tilde{k}_s = \frac{2\sqrt{2E}}{(2-\nu)(1+\nu)}\left(R_{ij}\xi_{ij}\right)^{1/2} \tag{5}$$

If $F_{ij}^{s} < \mu F_{ij}^{n}$ then the tangential movement between the centers of the two grains is opposed by a growing elastic force. Once the Coulomb failure criterion is reached "sliding" (inelastic tangential movement) occurs (Goren et al., 2010), and the resisting force does not grow.

The motion of each grain is a result of the forces it has between surrounding grains. The forces calculated from eqs. (2 & 4) are used in the momentum equations for grain i :

$$m_i \dot{\boldsymbol{u}}_{\boldsymbol{i}} = m_i \boldsymbol{g} + \sum_j \boldsymbol{F}_{\boldsymbol{ij}} - \frac{\nabla P \cdot V_i}{1 -} \tag{6}$$

$$I_i \dot{\boldsymbol{w}}_{\boldsymbol{i}} = \sum_j R_i \, \hat{\boldsymbol{n}}_{\boldsymbol{ij}} \times \boldsymbol{F}_{\boldsymbol{ij}} \tag{7}$$

where $\dot{u}_i$ is the translational velocity vector time derivative, and $\dot{w}_i$ is the rotational velocity vector for grain i , g is the gravitational acceleration, m_i is the grain's mass, I_i is the grain's moment of inertia, and F_{ij} is the force at the contact between grains i and j.

The last term in equation (6) represents the drag force exerted on grain *i* by the pressure gradient, ∇P, which is normalized by the solid fraction, $(1 - \quad)$, in its vicinity. Here is the local porosity, and V_i is the volume of grain *i*, (Goren et al., 2010, McNamara et al., 2000).

2.1 PORE FLUID AND GRAINS: A TWO-PHASE MODEL

The next step in the evolution of the model was to add the effect of fluid motion into the system. This addition by Goren et al, 2010, uses the mass conservation laws as applied to a two-phase continuum governed by:

$$\frac{\partial[(1 - \quad)\rho_s]}{\partial t} + \nabla \cdot [(1 - \quad)\rho_s u_s] = 0 \tag{8}$$

$$\frac{\partial\left[\quad \rho_f\right]}{\partial t} + \nabla \cdot \left[\quad \rho_f u_f\right] = 0 \tag{9}$$

Here *t* is time, the densities of the solid and fluid are ρ_s and ρ_f, u_f is the velocity field of the fluid, and u_s is the local velocities of the grain velocities. In densely packed systems, fluid inertia is negligible, so the flow can be modeled by Darcy's Law:

$$\left(u_f - u_s\right) = -\frac{k}{\eta}\nabla P \tag{10}$$

where *k* is the permeability of the granular matrix, η is the fluid viscosity, and *P* is the excess fluid pressure over hydrostatic. The fluid density is given by the fluid state equation:

$$\rho_f = \rho_0(1 + \beta P) \tag{11}$$

Here β is the adiabatic fluid compressibility, and ρ_0 is the fluid density at hydrostatic pressure. We then combine equations 8-11 to give an equation for pressure (Goren et al. 2010).

$$\frac{\partial P}{\partial t} = \frac{1}{\beta}\nabla \cdot \left[(1+\beta P)\frac{\mathrm{k}}{\eta}\nabla P\right] + \frac{(1+\beta P)}{\beta}\nabla \cdot u_s \tag{12}$$

In the work of Goren et al., 2010, they assumed pressures attained in the system would be small enough that $\beta P \ll 1$, so this term was neglected from equation 12. However, our results show that this assumption is only valid for systems with high internal permeabilities. As the system's internal permeability decreases the pressures will increase. If this term is ignored, pressures will not respond to imbalances between the source and diffusion terms at the correct rate when the pore pressures become very positive or negative. It is due to these negative effects that we will include this term in the pressure solution for this paper. There is a finite grid spacing imposed on the system, which is used to calculate pressure perturbations within the gouge material. The grid size is set to ~2 grains in height.

The first term of equation 12 gives the temporal evolution of pore pressure, the second shows the pore pressure diffusion due to fluid flow, and the third term is a source for pore pressure changes that are present due to the changes in pore volume. The third term is related to the local rate of change in porosity, and can be described as a local volume strain. When the strain rate is positive, the pore volume expands allowing the fluid to flow into the expanding pore volume as the fluid depressurizes. When the strain rate is negative, the pore volume decreases, and the fluid flows out of the compressing pores. A final term describing the advection of pore pressure by the movement of the

grain matrix is small and has been neglected. Equation 12 can be non-dimensionalized to illuminate a controlling parameter on the evolution of the pressure, De:

$$\frac{\partial P'}{\partial t'} = \frac{1}{De}\frac{1}{\Phi'}\nabla \cdot [(1 + E\beta P')\mathrm{k}\,\nabla P'] - \frac{(1 + E\beta P')}{\Phi'}\nabla \cdot \vec{\mu}'_s \tag{13}$$

Here the dimensionless Deborah number gives the ratio between the time scale for the pressure to relax via porous flow and the time scale for the generation of pressure by compaction/dilation events.

$$De = \frac{{}^{2}/_{\mathrm{D}}}{/_{\mathrm{u_o}}} = \frac{t_{diffusion}}{t_{generation}} \tag{14}$$

Where D is the diffusivity of pressure $D = \frac{k_o}{\beta\eta d_o}$ and ℓ is the distance from the pressure generating event (a region of shear localization) to the boundary of the system. When De <<1 the pore pressures can easily diffuse from the shearing region to the boundaries within the time scale of deformation. When De $\gg 1$, the pore pressure diffusion from the shearing row does not reach the boundaries. In this case, the pore pressure is indifferent to the drainage conditions applied on the boundaries.

We find the relationship between porosity and permeability through a 2D version of the Carmen-Kozeny relationship. In our model we follow the relationship used in Goren et al. 2010, which used the area of disks to find permeability instead of the volume fraction of spheres. Using this 2D mapping gives the following relationship for permeability:

$$k = k_c \frac{\bar{d}^2}{540}\frac{(1 + 2\Phi)^3}{(1 - \Phi)^2}$$

where Φ is the local 2D porosity, $\bar{d}^2$ is the mean local grain size, and k_c is a prefactor (Goren et al. 2010, McNamara et al. 2010). We vary the prefactor to simulate gouge with different mean permeabilities. In a particular experiment the prefactor is held constant, but both local grain size and porosity can vary in time and space.

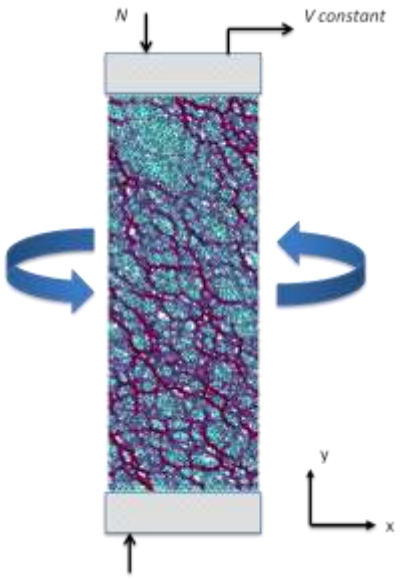

Figure 1 A general representation of a 24 x 70 grain material with a horizontally periodic granular layer. The thickness of the black lines denote the magnitude of the contact forces between grains, and the color of a grain shows the magnitude of total contact forces on that grain. The top and bottom walls consist of glued half grains with different radii. The top wall is pulled to the right with a constant velocity *Vsp*. Under right-lateral shear stress, the network of force chains is preferentially oriented in the direction of maximum principle stress.

3. MODEL SETUP

We conducted a large suite of numerical experiments under a range of conditions. Each experimented is conducted in a model gouge layer that is ~70 grains thick, confined by the top and bottom semi-rough walls, which consist of bonded grains with varying diameters (Figure 1). This thickness is chosen because we find that shear tends to localize in zones 8-10 grains thick, so this size is required to allow shear zones that are not strongly affected by the boundary. The along-axis period (width of the experiment) is 24 grains. The width is relatively small only to reduce the computational cost of the experiments.

Table 1. Experimental parameters used in each of the numerical simulations.

Parameters	***Description***	***Nondimensionalized values***	***Dimensional***
V	*Shear velocity*	10^{-3}, 3×10^{-4}, 10^{-4}	0.6, 1.8, 6.0 ($^{m}/_{s}$)
N	*Effective confining stress*	10^{-3}, 3×10^{-4}, 10^{-4}, 3×10^{-5}, 10^{-5}	0.8, 2.4, 8, 24, 80 (*Mpa*)
De	*Deborah number*	0.1, 0.3, 1, 3, 10	N/A
Box size	*Measured in grain height (~1mm)*	24x70	N/A
k_c	*Internal permeability of gouge layer*	10^{-5}, 10^{-6}	10^{-14}, 10^{-15} (m^2)

For each experiment, a set of grains is created that have diameters ranging from 0.8 to 1.2 times the mean diameter, taken to be 1 mm. Once the grains have been created and packed between the walls, a stress normal to the top wall, N, is applied to compact the grains while the bottom wall remains fixed in place. Due to the periodicity of the system, this creates an approximately isotropic effective confining pressure, N,. Gravity is not applied to the model. In each of the simulations we apply a constant horizontal shearing velocity, V, to the top wall of the system, while keeping the bottom wall fixed. Experiments were conducted with different values of V and N, and the imposed

Table 2. Description of the material constants used in model.

Symbols	*Description*	*Values*
β	*Fluid compressibility*	$4.5 \times 10^{-10}\ Pa^{-1}$
η	*Fluid viscosity*	$10^{-3}\ Pa\ s$
ρ_f	*Density of pore fluid*	$1000\ {}^{kg}/_{m^3}$
ρ_s	*Density of the bulk material of grains*	$2460\ {}^{kg}/_{m^3}$
μ	*Friction coefficient*	0.5
d	*Grain diameter*	$5 \times 10^{-4}\ m$
E	*Young's Modulus*	$8 \times 10^{10}\ Pa$
υ	*Poisson's Ratio*	0.2

permeability constant, k_c, (Table 1) while all other material properties were kept constant (Table 2). The computer code and its input and output are non-dimensionalized. All lengths are scaled by the mean grain size, stresses are scaled by the Young's modulus of a grain, and velocities are scaled by the P-wave velocity in a grain. The input parameters of the systems, N, V and system size, are referred to in the paper are the scaled, dimensionless values. If we take the grains to be quartz, then the stress and velocity scales are 80 GPa and 6700 m/s. Therefore the shear velocities that we will examine in this study are comparable to earthquake slip velocities (0.6 to 6 m/s), and the applied effective confining stresses range from 0.8 to 80 MPa. The mean permeabilities in the two systems examined are on the order of 10^{-14} and 10^{-15} m^2.

As noted in other works (Aharonov et al., 2002, Shojaaee et al., 2012) there is an initial transient behavior when the packed stationary system first begins to shear, before the systems settles into a quasi-steady patterns. In order to study the steady-state behavior of the systems we ran each of experiment without fluid for a shear strain of 10. From that point, we ran the model including the pressure equation, but assumed that pressure was fully equilibrated at a strain of 10 (internal pressure set to the fixed boundary value). The system was then run for a further strain of 10 before we began to analyze the results of each run so as not to confuse our data with any transient behaviors depending on the shearing conditions. We extended a few selected experiments to a strain of 100 to ensure that a strain of 20 was sufficient, and saw no qualitative change in steady state shear behavior.

4. RESULTS

The pressure deviations created during shear will increase in systems with increased De$\left(\propto \frac{V}{k}\right)$. This is expected because higher V will generate more compaction and dilation events in a shorter time, and lower k restricts fluid flow which make it more difficult for changes in pressure to equilibrate. Goren et al (2010) predicts that for shear localized to a plane, the maximum pressures generated will vary with De for De$\ll$1 and with $\sqrt{De}$ for De$\sim\vartheta$(1), as is the case for our experiments. Pressure deviations can only effect the grains if they overcome the contact forces, which are proportional to the mean effective confining stress, N. Therefore, we expect that the effect of fluid will be greater when ΔP becomes a significant fraction of N. So the effects of fluid will correlate positively with *V* and negatively with *N* and *k*. We see these characteristics in our experiments, but will explore the relationship in more detail in section 5.

4.1 POROSITY AND SHEAR

Shear of a granular system requires dilation to allow grains to move around each other. The ease with which dilation can occur will thus directly effect the overall rheology of the granular material. Once a system begins to shear, it will dilate from its original packed state to a higher preferred mean porosity. In general, faster shear requires a higher mean porosity. Figure 2 shows the evolution of porosity in the dry systems after shear begins. The dilation from the rest state to the dilated steady-state occurs over a shear strain of about 2-3.

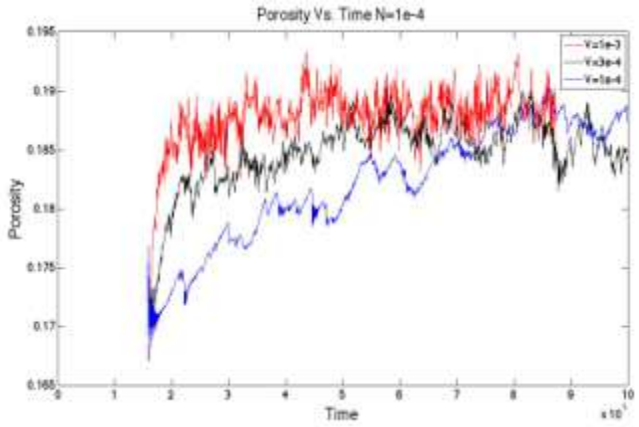

Figure 2 Porosity vs. dimensionless time for three dry systems with the same values of *N* and different values of *V*. Each system starts from a compact state with no shear stress and low porosity. Systems with different *V* will reach slightly different steady-state porosities, over a similar strain of ~2-3.

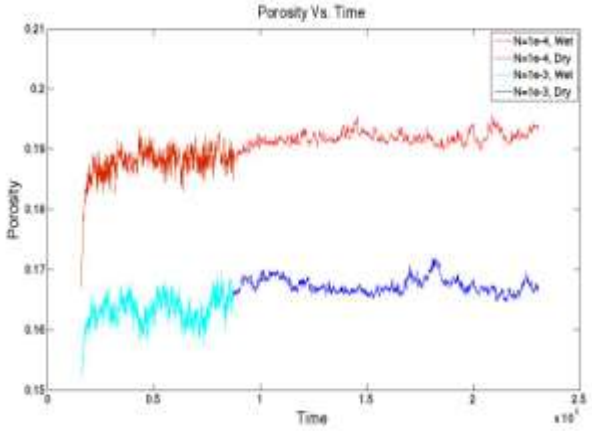

Figure 3 Porosity vs. dimensionless time during dry shear and with fluid (k_c=10^{-5}) for two different values of *N*. The porosity will increase when fluid is added to a higher steady-state, while the amplitudes of the fluctuations in porosity will decrease as a result of the pressures being generated during compaction/dilation events.

After a strain of 10, fluid is "added" to the dry systems. Figure 3 shows that the amplitude of the fluctuations in porosity are reduced after fluid effects are included. This

behavior is attributed to the generation of positive/negative pore pressures that occur during compaction/dilation events. As the system dilates, negative pressures are created inside the pore spaces which will pull in fluid into the newly opened void space, and as the system compacts positive pressures are created as the fluid is pushed out of the pore space into neighboring rock. Since flow into and out of the layer will act as a damping force on the vertical motion of the wall, this reduces variability in porosity. Figure 3 also shows that mean porosity is higher after fluid is added. At a higher overall porosity, the permeability of the gouge layer is higher, which enhances fluid flow. Therefore, fluid systems will typically shear at higher mean porosity than dry. This mean porosity is usually larger for higher values of the imposed permeability constant, k_c.

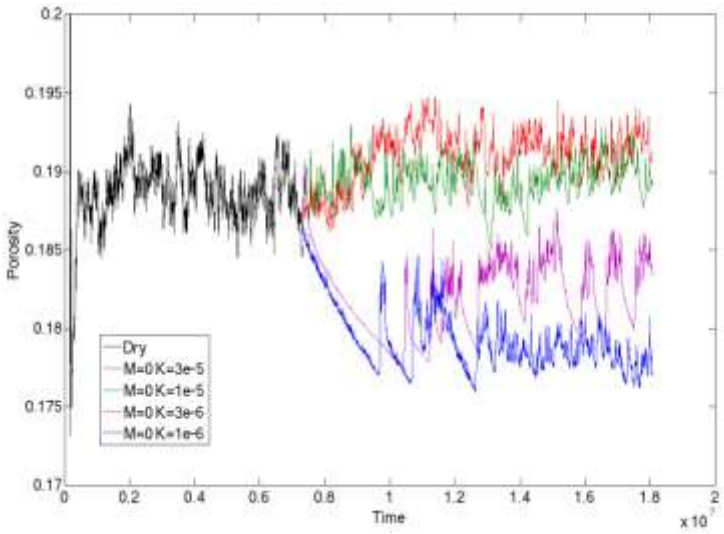

Figure 4 Porosity vs. dimensionless time during dry shear and with fluid for N=10^{-5} and V=10^{-4} but with different k_c. We see that systems with lower k_c will have steady-state porosity values lower than the dry systems, and they will collapse toward this low porosity if started from a dilated dry state.

For some simulations with low V, N, and $k_c=10^{-6}$, mean porosity is much lower, even than dry simulations. These conditions are marked by frequent liquefaction events, during which all shear strength is lost and the system compacts. This behavior drives the system to lower mean porosity, both during and in-between these liquefied states. Under these conditions, if fluid is added to a sheared dry system, then the collapse toward the new steady-state porosity is dramatic (Figure 4). If fluid is instead added to densely packed relaxed state, the system will quickly dilate to the same low porosity without the major liquefaction events. The role of liquefaction will be discussed in more detail in a later section, but its affects on some simulations are noted in the following plots.

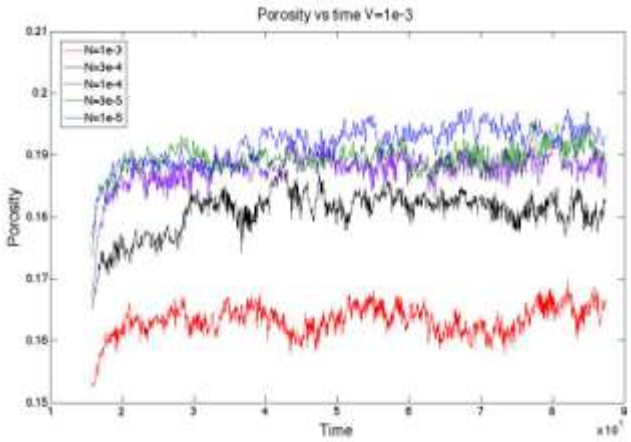

Figure 5 Porosity vs. dimensionless time during shear with fluid for $k_c=10^{-5}$ and $V=10^{-4}$ and a range of N values. Systems with lower values of N, will reach a higher steady-state mean porosity, approaching the critical porosity for a system that can have lasting force chains (~0.20).

The values of the resulting mean steady-state porosity show a large dependence on the effective confining stress, N, and a smaller dependence on shear velocity, V. Systems with low values of N have higher mean porosity than systems with high N

(Figure 5). At very low normal stress (depending on the shear velocity) the system will dilate until grains no longer maintain continuous contacts and become liquefied. These results agree with Aharonov et al. 1999, which shows that once the normal stress becomes low enough, the grains will lose the contact forces between grains (at a porosity of about 22%) and the wall boundaries can shear without influencing the grains.

Figure 6 shows the mean porosity of each of our simulations vs. the effective confining stress on the system. Fluid-saturated systems will have a higher mean porosity during shear than dry systems, except in simulations with frequent liquefaction. The mean porosity decreases by about 1% with increasing N, up to $N=3 \times 10^{-4}$. (The much lower porosity in $N=10^{-3}$ runs indicates that there is beginning to be some unrealistic overlaps between grains in model, so N cannot be further increased). This trend is reversed for liquefied systems, since liquefaction is preferred at low N.

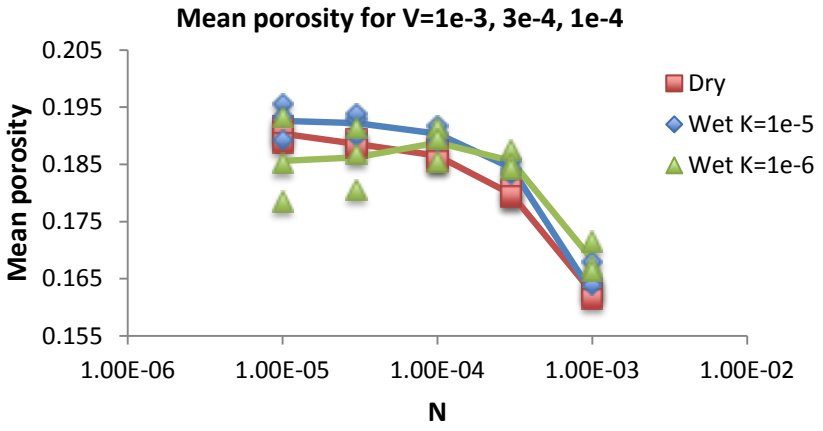

Figure 6 Mean porosity (averaged over strains of 20) vs. the effective confining stress for various systems. In most cases, mean porosity decreases with increasing N, and fluid systems typically have higher mean porosity than the dry systems. The exceptions are systems with low N and low k_c. These deviations are attributed to the occurrence of liquefaction events during which porosity is reduced.

Figure 7 shows plots of the mean porosity for each of the dry systems vs. the shear velocity, and it is seen here that the values of mean porosity typically do not change more than 0.3-0.4% as we increase/decrease velocity. Figures 8.a and 8.b show that velocity has the same effect in the fluid runs, although the effect is slightly larger. The liquefied runs in this case accentuate this trend, since liquefaction events last longer in the lower *V* simulations.

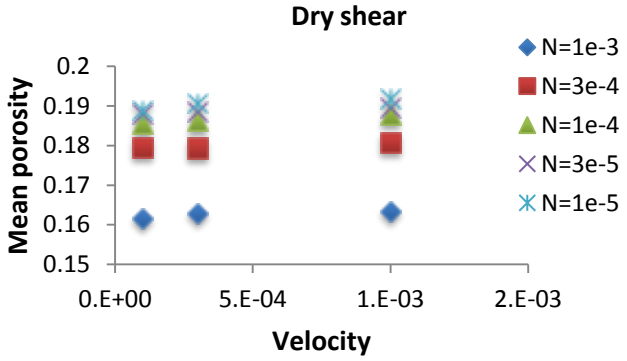

Figure 7 Mean porosity vs. shear velocity plot for dry systems. Here we see that higher shear velocity typically causes higher mean porosity, but the effect is not large.

4.2 LOCALIZATION

It has been previously shown (Aharonov and Sparks 2004, Antonellini and Plloard 1994, Jian-Fei Chan et al., 2010, Kock and Huhn 2007, Shojaaee et al., 2012) that shear is not concentrated across a single layer of grains, but occurs in bands ranging from a few grains wide (localized shear), to the entire layer (homogenous shear). Localized shear can occur at different positions within the layer, and may persist in a location for a short period (displacement of only a few grains) or indefinitely. We divide

the system into shear-paralleled strips about two grains thick, and use the average the layer-parallel velocity (V_x) to create velocity profiles across the layer. Figure 9 shows both instantaneous profiles and time-averaged ones. There are three distinct patters of shear patterns: (I) homogeneous shear, (II) transient random localization, and (III) persistent boundary localization. A given simulation will show one of these patterns, or a transitional state between two of them, depending on the parameters imposed on the system. Time-averaged velocity profiles (Figure 9.d) can clearly distinguish systems with persistent boundary localization.

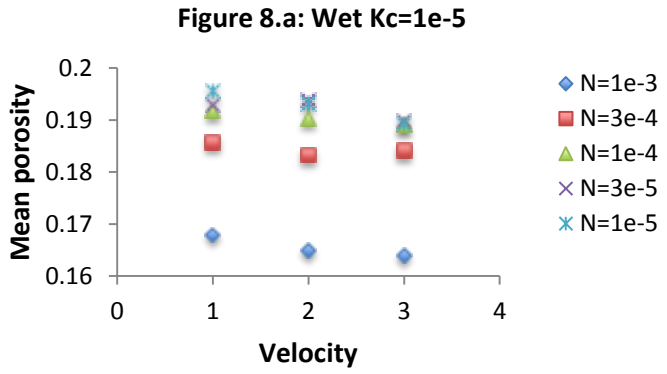

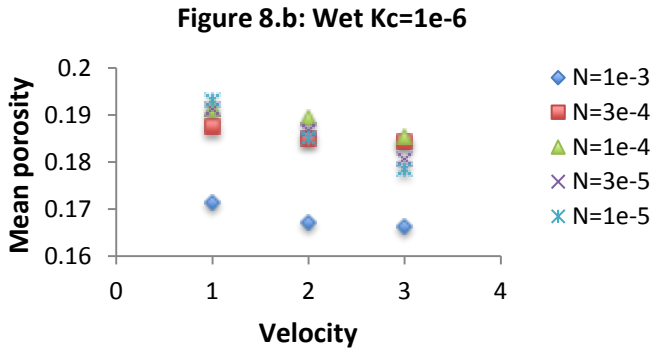

Figure 8 Mean porosity vs. shear velocity for fluid systems with (a) k_c=10^{-5}. and (b) k_c=10^{-6}. Similar to Figure 7, we see the same effect of shear velocity on mean porosity, even though the effect is slightly than in dry systems. Mean porosity is reduced in low *V* simulations with significant liquefaction.

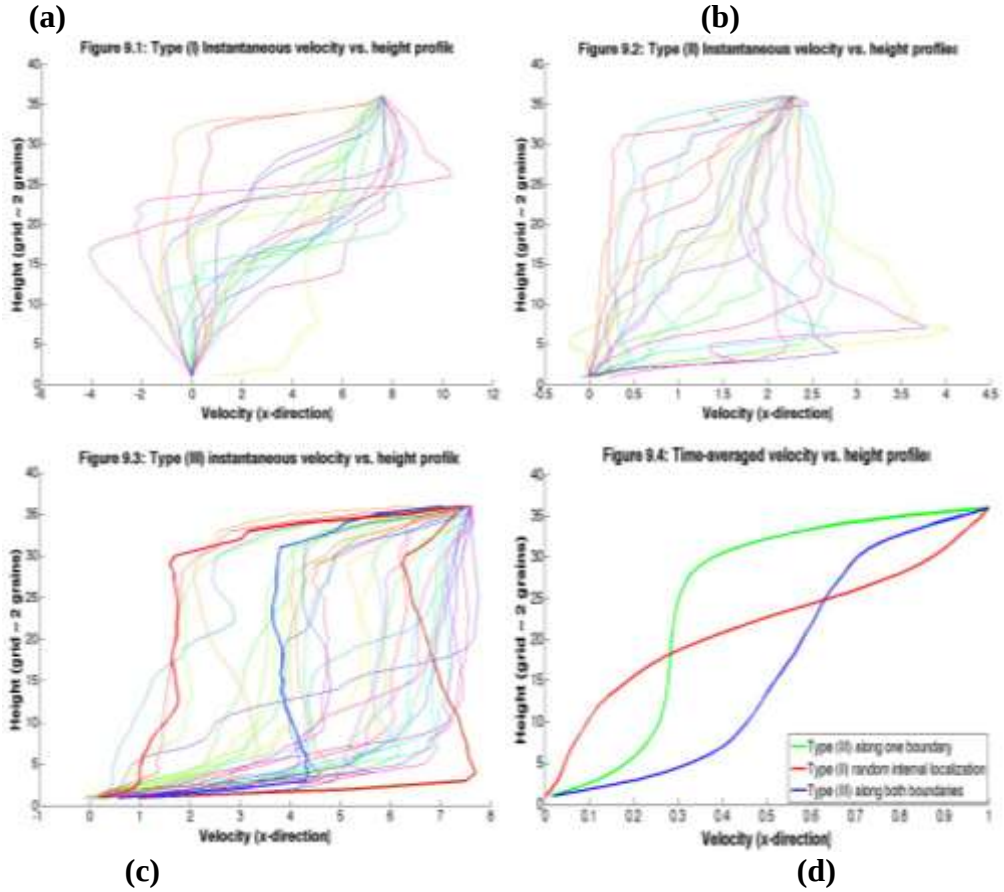

Figure 9 Instantaneous layer-parallel velocity vs. height profiles exhibiting typical (a) type (II) shear with shifting internal shear bands (b) type (II-III) shear, with shifting shear bands that have a preference for the boundaries, and (c) type (III) shear, boundary localized systems. Each plot contains many instantaneous profiles at different times, which converge to *V* at the top of the profiles. (d) Time-averaged versions of the profiles in parts (a-c). The internally localized system (a) averages to an almost linear profile, as would be expected in a uniformly shearing system without shear bands. Whereas the boundary localized time average plot has a far from linear trend towards either boundary.

However, systems with type I or type II behavior will have similar time-averaged patterns. Each panel of Figures 9.a-c, shows a group of instantaneous profiles at different times for simulations undergoing type II, a transitional mixture of types II and III, and type III shear, respectively. Figure 9.a shows transient shear bands forming in

four different places ranging from the middle to the boundary. Figure 9.b shows several shear bands, with most shear occurring near the boundary. Figure 9.c shows a system dominated by boundary shear. The boundary localized systems are unique in that the localization can persist along one boundary for long shear strains, rapidly alternate between boundaries, or occur on both boundaries simultaneously.

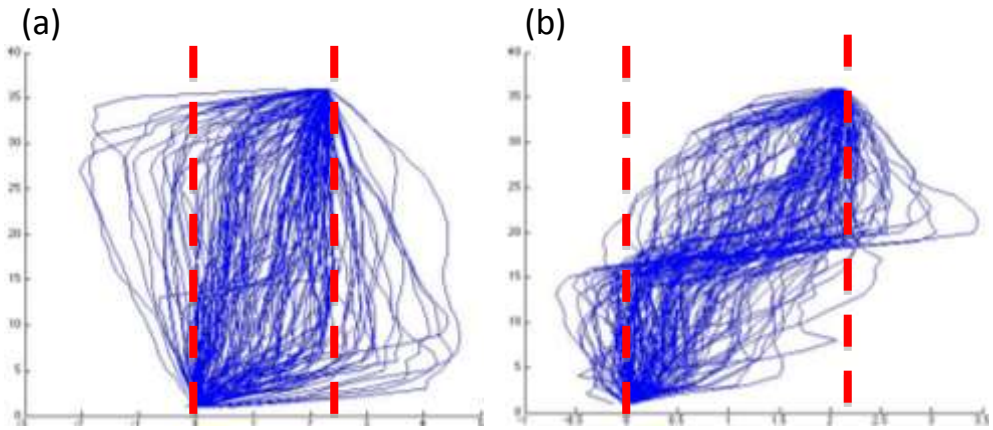

Figure 10. Instantaneous velocity vs. height profiles for two systems undergoing (a) boundary localization and (b) internal localization shear. In both systems, the majority of the velocities range from 0 to the top wall velocity. However, the velocities outside of these bounds are a result of an elastic rebound-like effect in slip on a shear band suddenly releases store elastic energy from deformed blocks above and below a shear band

During localized shear, the velocity in the shear band varies from zero to the wall velocity over 4-5 stripes (8-10 grains), with the region below nearly motionless and the region above moving at the wall velocity. Under some conditions (typically high N) there can be instantaneous velocities at the edges of the shear band that go above and below these bounds (Figures 9.a and 10). These high velocities are shown to occur as the

frictional forces on grains in a particular layer are overcome by the shearing forces on the grains which cause the blocks outside the shear band snap forward and backward, in an elastic rebound effect. When this occurs, the velocity gradient across the shear band is quite high, while the shear band thickness is still 8-10 grains.

4.2.1 DRY SYSTEMS

To observe the transitional behavior between types (I-III) shear we use grid layer averaged shear strain rate plots. At intervals, the model averages the velocity difference across each horizontal grid layer. A sequence of these instantaneous averages are then displayed as adjacent color columns to show how the distribution of shear strain evolves with strain. Note that the horizontal axis in each figure is not time, but total strain (from 10 to 20), so simulations with different driving velocities will represent different total times. Figure 11 show strain-rate evolution plots for 15 different dry experiments are arranged in a "phase diagram" according to the imposed effective confining stress, N, and top wall velocity, V used in each simulation.

Figure 11 shows the transition from type II to type III to type I as V/N increases. As V/N increases, the shear bands begin to form preferentially toward the boundaries of the box (transition from type II to type III). During type III shear the shear bands will locate toward one of the boundaries and will not exhibit a back-and-forth pattern between the walls. As V/N increases beyond 100, shear becomes less localized and the system approaches distributed shear (type I). These findings are consistent with the work of Shojaaee et al., 2012, which describes this transitional behavior for dry shear systems.

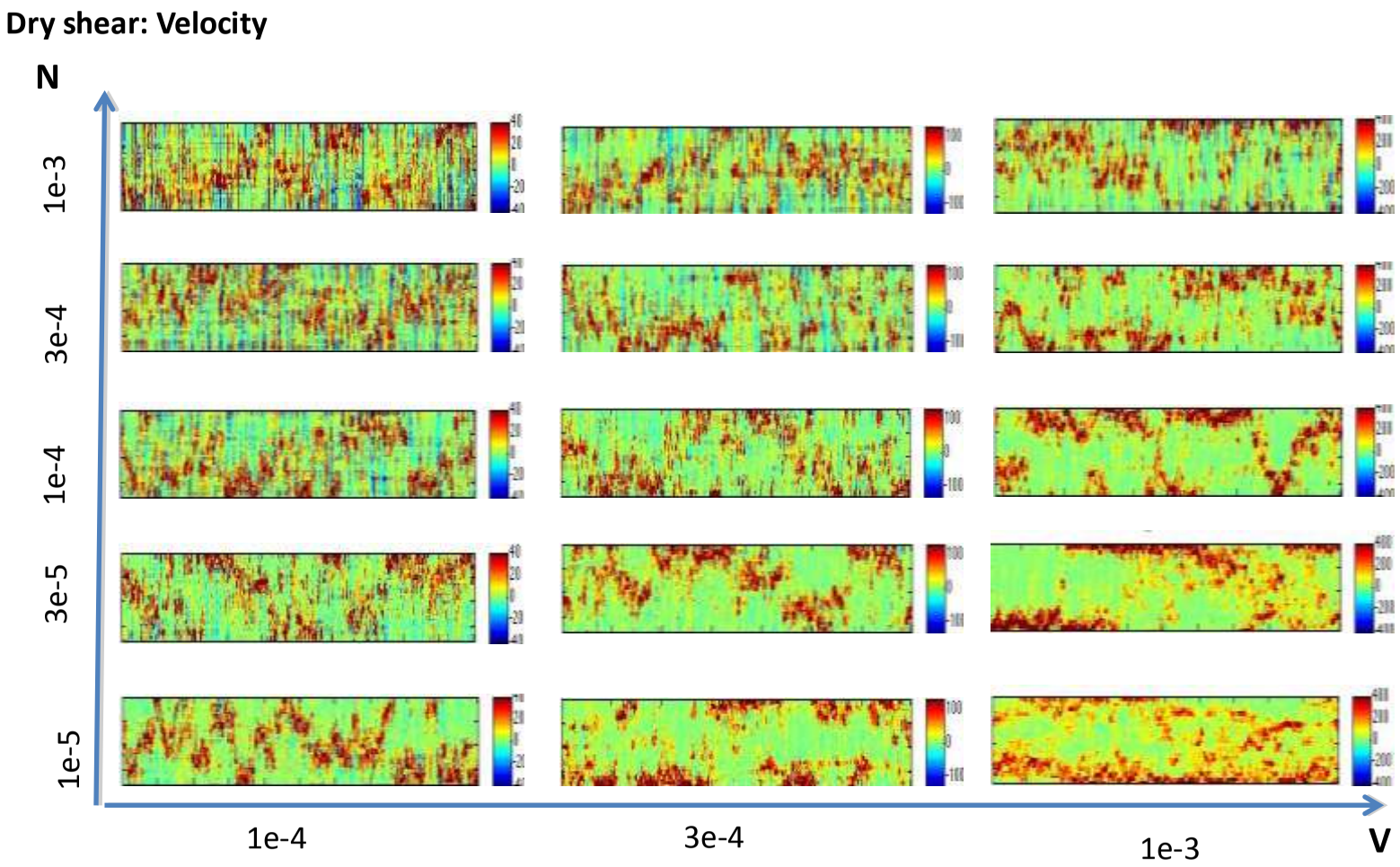

Figure 11 Shear strain rate profiles vs. shear strain for 15 dry simulations arranged according to the *N* and *V* for in each simulation. Red colors denote areas of high strain rate (shear bands). We see the transitional behavior between types (IIII and II) shear as *V/N* decreases.

To quantify the changes in shear behavior we calculated the magnitude of localization, M_L. M_L is the time average of the largest velocity differential between two adjacent grid layers ($\langle \Delta V_{max} \rangle$) divided by the change in velocity expected for a uniformly shearing system, scaled by *n*, the number of strips in the system:

$$M_L = \frac{\langle \Delta V_{max} \rangle}{\left(V_{top\ wall} - V_{bottom\ wall}\right)/n}$$

Using this factor we get a closer look at the magnitude of the shearing strain rate, even though the values given will be altered during times of large elastic slip events. When M_L=0 the system will undergo type (I) distributed shear over the whole system, and as $M_L \rightarrow$n the number of strips that are shearing will decrease. Figure 12.a shows that localization gets stronger with decreasing *V/N*, and it is only at the highest *V/N* that we begin to see more of a type (I) shear ($M_L < 5$). Very high values of M_L (≥ 10) that are found at low *V/N* are not the result of continued concentration of shear, but are actually reflections of elastic rebound between shearing bands as described in section 4.1 (Figure 10.a).

We then calculated a modified version of M_L to account for the large rebound events discussed above. Here we take the time average of the maximum velocity differential divided by the difference between the maximum and minimum velocities at the same instant in time, scaled by the number of layers in the system.

$$M_L^* = \left\langle \frac{\Delta V_{max}}{\left(V_{max} - V_{min}\right)/n} \right\rangle$$

Using M_L^* to calculate the amount of localization that is present in the system will limit the effects of the large rebound events giving a more accurate view of how localized shear is. In rebound events, V_{max} may be larger than $V_{top\ wall}$, while $V_{min} < V_{bottom\ wall}$, so $M_L^* \leq M_L$. Since we are scaling this factor the same as M_L the values will

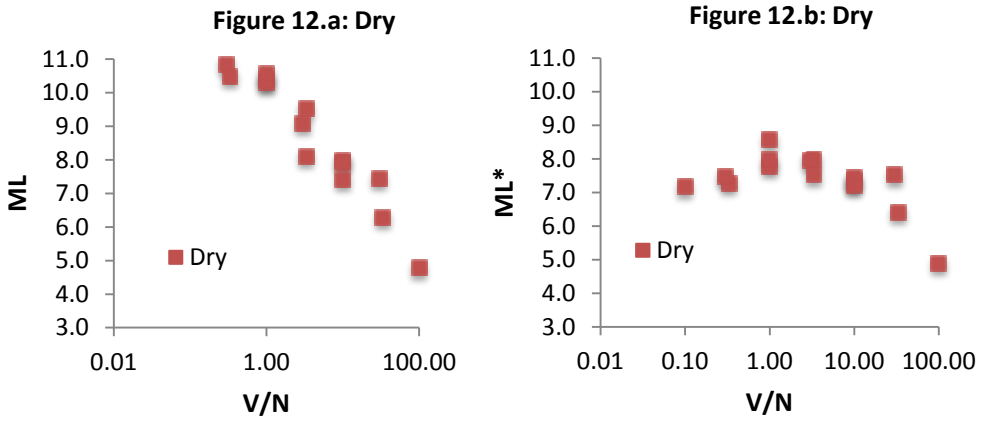

Figure 12 Two measures of the magnitude of localization, (a) M_L and (b) M_L^* (see text) vs. *V*/*N* for 15 dry simulations. Here we see localization increases with decreasing *V*/*N*, however the high M_L values are representative of high velocities caused by elastic rebound around shear bands. The relatively constant values of M_L^*~7-8 indicate that the thickness of shear bands is roughly independent of *V*/*N*, except at the highest *V*/*N*, where shear is not well-localized.

represent the same localizing trends. Figure 12.b shows that M_L^* holds constant at ~7-8 for all *V/N* except at high *V* simulations that show a decrease in localization. This shows that localized shear bands under all conditions represent the same localizing trends. Figure 12.b shows that M_L^* holds constant at ~7-8 for all *V/N* except at high *V* simulations that show a decrease in localization. This shows that localized shear bands under all conditions are confined to about 1/8th of the entire layer thickness, or a band

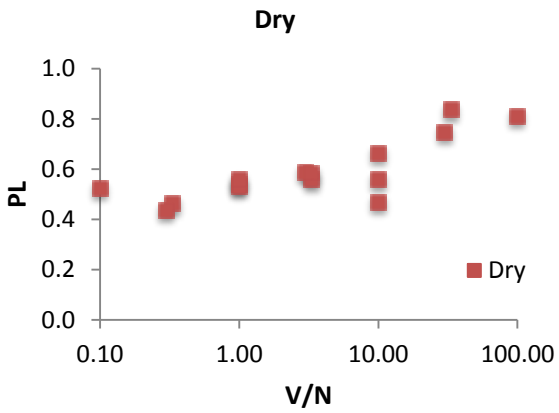

Figure 13 The position of localization, P_L (see text), vs. *V/N* for dry simulations. P_L will transition from type II (~0.5) to type III (~1.0) shear as *V/N* increases. The tendency of dry simulations to localize on the boundary at higher shear rates and/or low confining stresses is a characteristic of the grain and boundary properties. At the highest *V/N* the value of P_L is less meaningful, because this simulation is not purely localized shear.

~8-10 grains thick. These findings are consistent with previous works (Aharonov et al. 2004, Goren et al. 2010, Shojaaee et al. 2012, Tejchman and Wu 2009) performed on dry systems undergoing constant shear.

In order to quantify the position of localized shear we begin by finding y'_{max}, which is the time-averaged position of ΔV_{max} , scaled by the thickness of the layer.

$$P_L = 2\left|y'_{max} - \frac{1}{2}\right|$$

Here P_L gives the time-averaged position of maximum shear relative to the middle of the box. If P_L=1 the shear bands will occur along one or both of the boundaries (type I), while P_L=0 means shear is fixed in the middle of the system. If shear bands shift randomly within the layer between the middle and boundary (type II) , P_L=0.5 Figure 13 shows that P_L changes from type II to type III with increasing *V/N*. At the highest values

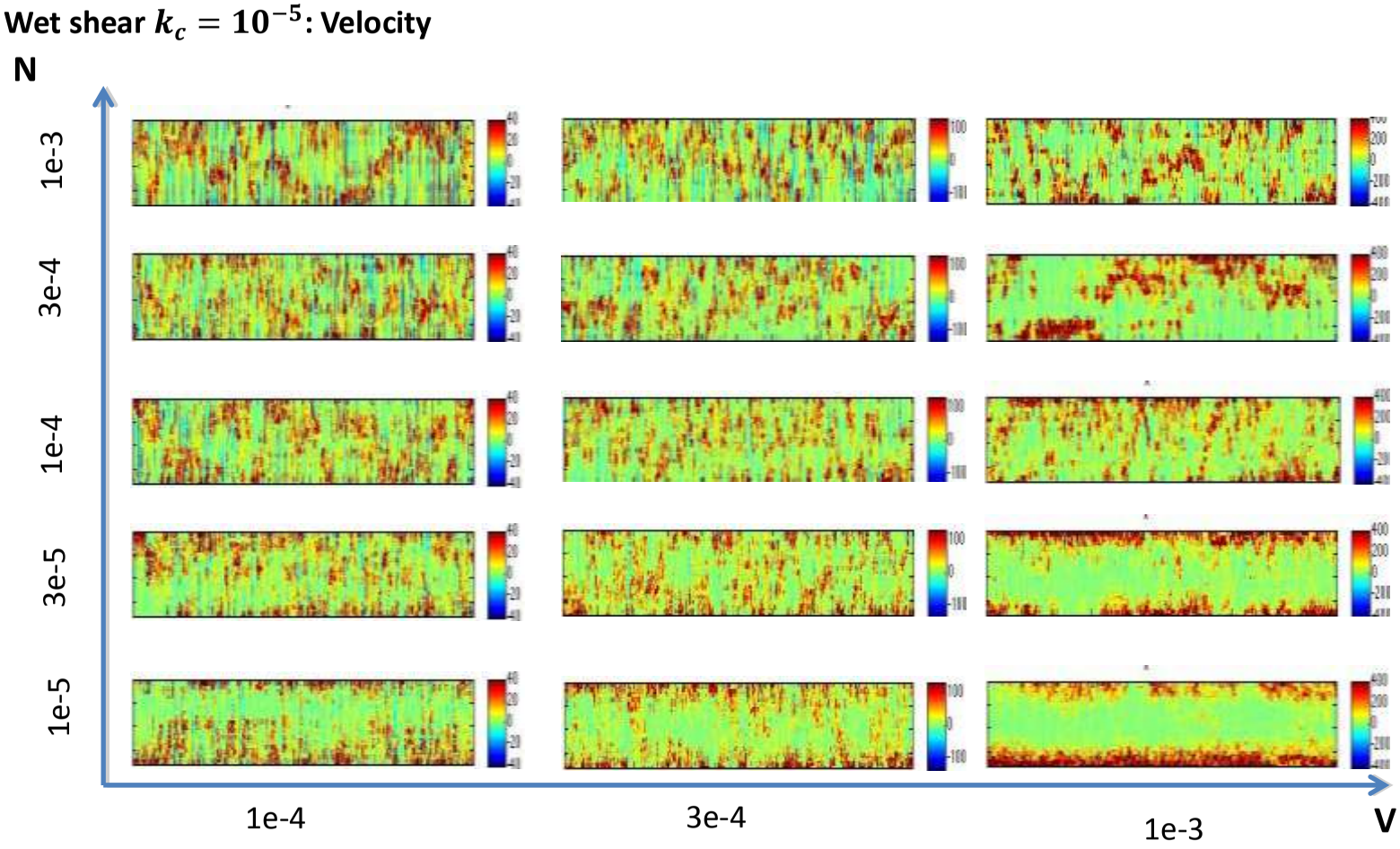

Figure 14 Porosity profiles vs. shear strain for the dry simulations, arranged similarly to Figure 11. The largest effect is the overall porosity dependence on *N*. For systems undergoing type (III) shear, less grain rearrangement occurs in the interior of the gouge, resulting in porosity patterns that stay constant for large strains (long periods of shear).

of *V/N* we can see some randomness that is present due to the fact that P_L is only meaningful for localized systems.

If we look at the changes in porosity during these events we can also see the dilatancy patterns that occur along the boundaries as *V/N* increases. Figure 14 shows a phase diagram similar to Figure 11, showing evolution of the layer averaged of porosity for all the dry simulations. It is shown that the effects of shearing on porosity are more effected by variations in normal stress than on changes in wall velocity (Figure 14). As *N* decreases the porosity increases, with the larger porosity starting at the boundaries for $N = 10^{-5}$, and moving further into the gouge layer for $N = 10^{-4}$. Since we use a 2-D version of the Carmen-Kozeny relationship, the values of porosity seen in Figure 14 are not indicative of a natural granular material, but rather are used to evaluate changes in porosity relative to the system.

4.2.2 WET SYSTEMS: $k_c = 10^{-5}$

This section describes a set of 15 simulations that included fluid with an internal permeability constant of 10^{-5} (permeability ~$10^{-14}\ m^2$). Each simulation was started from the end of the corresponding dry simulation and sheared to a strain of 20. All the data shown in this section comes from the second half of each simulation (strains 10 to 20). The shear strain rate plots of Figure 15 show that the transitional behavior between type II to type III shear remain the same for high/low *V/N*. However, in the fluid runs we see more type (III) shear occurring at lower values of *V/N* than the dry systems. The type (III) shear bands alternate between the top and bottom walls and are not as fixed to a single boundary. We also do not see the transition from type (III→I) within the range of

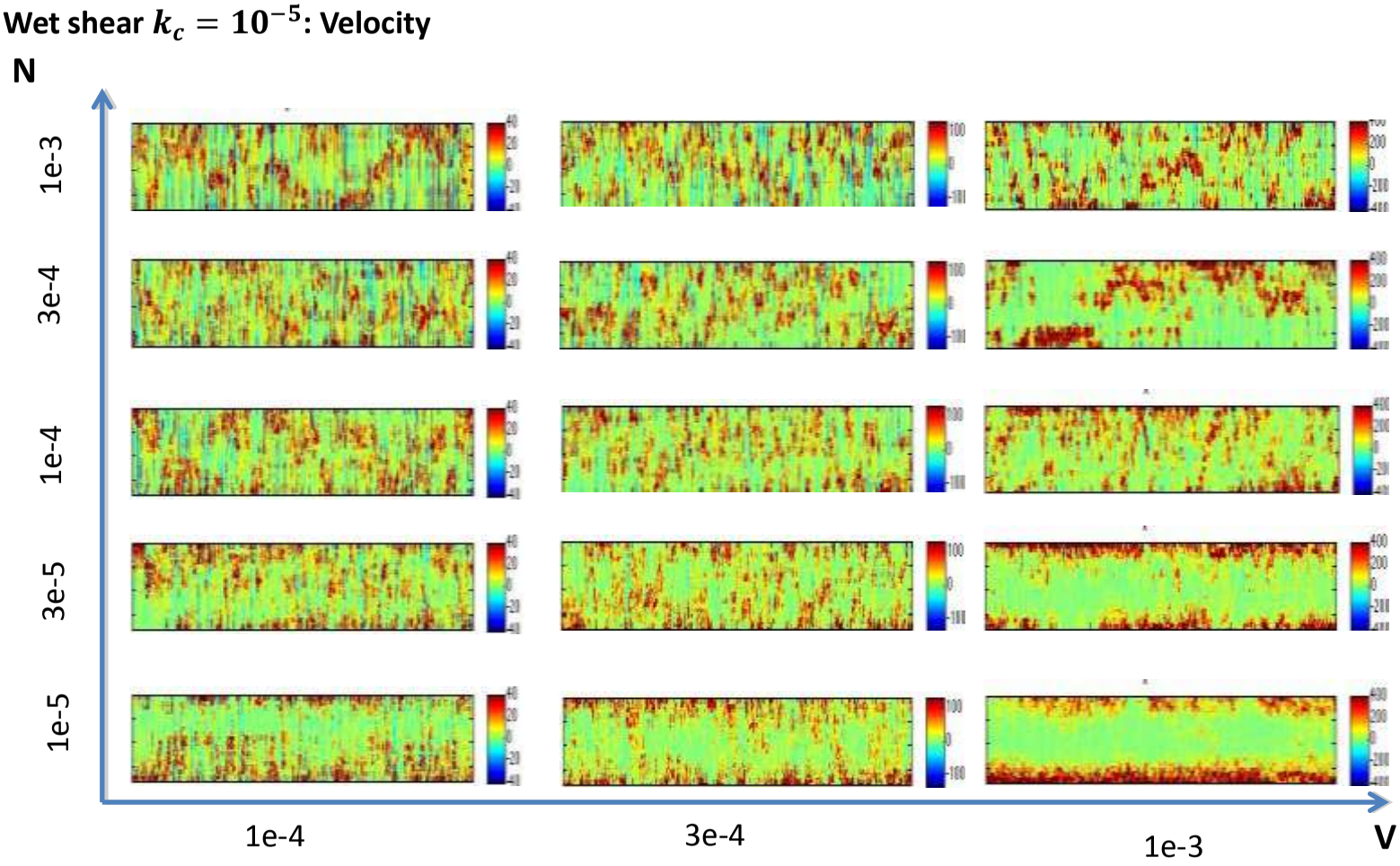

Figure 15 Shear strain rate profiles vs. shear strain for wet simulations with $k_c = 10^{-5}$, arranged similarly to Figure 11. We see similar transitions between types (II to III) shear as in the dry systems, but we lose the transition to type I at the highest *V/N*. Instead, shear in the wet systems continues to become more boundary-localized with increasing *V/N*.

V and *N* in Figure 15 that we see in the dry simulations. Looking at time averaged velocity plots (Figure 16), we see more pronounced boundary shearing trends for the wet vs. dry systems.

The M_L values show a constant localization ~7-8 for all *V/N*, which can be attributed to a decrease in the magnitude of rebound events in fluid saturated systems (Figure 17.a). The values for M_L^* remain constant at ~7-8 similarly to the dry systems except for the highest *V/N* where the dry systems become less localized (Figure 17.b). For P_L we see that the fluid saturated simulations trend with the dry except they are slightly more boundary localized (Figure 18). This relationship shows that the presence of fluid pressures will influence both the location of the shear bands and degree of localization of shear.

We see similar trends in the porosity phase diagram for wet shear as the overall dilation of the system seems to be more reliant on the normal stress applied to the system. The wet runs show an increase of porosity along the boundaries for systems with decreased values of *N* than in the dry simulations (Figure 19). As we compare porosity with increasing *V/N*, we see that the dilation along the boundaries is more pronounced, and there is a decrease in the amount of internal dilation present. We can also see a trend in the lower *V* and *N* systems, which follow the same boundary localized trends with *I*, but they begin to show large internal layers that remain in a compacted state throughout the experiment.

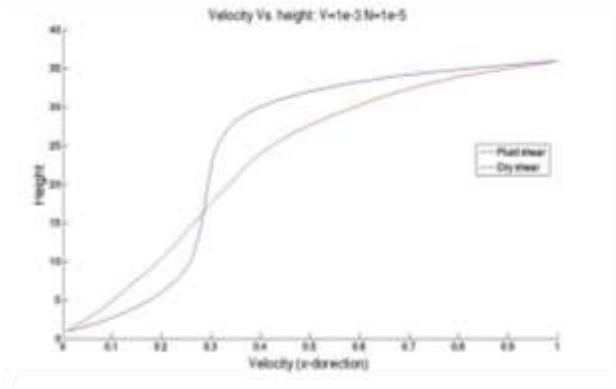

Figure 16 Time-averaged velocity profiles for dry and fluid experiments ($k_c = 10^{-5}$)with the same conditions (N=10^{-5}, V=10^{-3}). Fluid systems have more pronounced shear along the boundaries than dry shear systems.

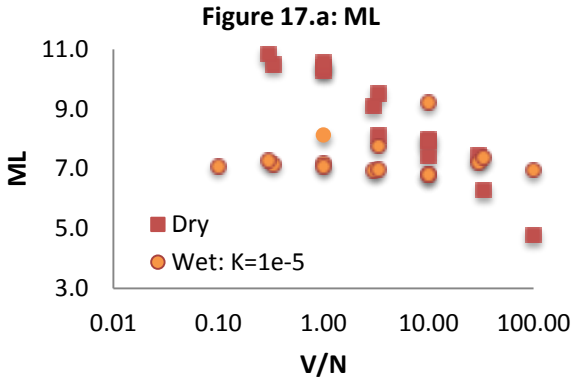

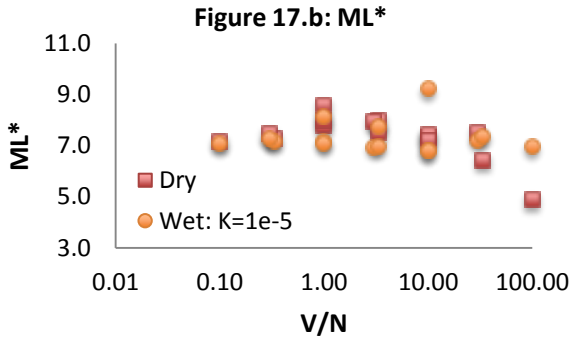

Figure 17 Two measures of the magnitude of localization, (a) M_L and (b) M_L^* vs. V/N for both dry and wet simulations with k_c=10^{-5}. The correspondence between the two measures shows that the elastic rebound effect is not very important in fluid saturated systems. The relatively constant value of M_L^* shows there is no transition to distributed shear at high V/N as in the dry system.

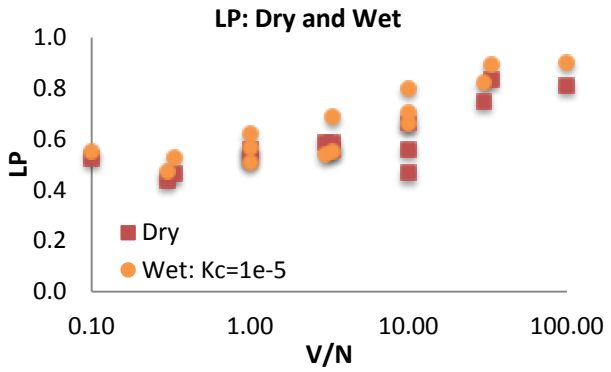

Figure 18. The position of localization, P_L vs. *V*/*N* for dry and wet (k_c=10^{-5}) simulations. The wet simulation P_L values show the same trend with *V*/*N* as the dry simulations, except are shifted slightly higher (stronger boundary localization).

Next we generated a phase diagram for pressure evolution within the gouge layer with the same parameters used in Figures 11 and 14. In each of the plots in Figure 20, ΔP is scaled by the *N* of that experiment to highlight the cases where fluid effects are important. In these plots ΔP is the deviation from the mean equilibrium pressure, and only plays an important role in the dynamics of the system as it approaches *N*. Here, we see in systems with decreased *N*, the pressures generated during shear can more easily reach and exceed *N*. The red bands represent compaction cycles, which increase ΔP as the system compacts faster than the fluid can flow out of the boundaries. These large pressures are then typically followed by large negative pressures generated as the system begins a dilation cycle. We can also see a higher percentage of liquefaction times with decreasing *N* and *V*.

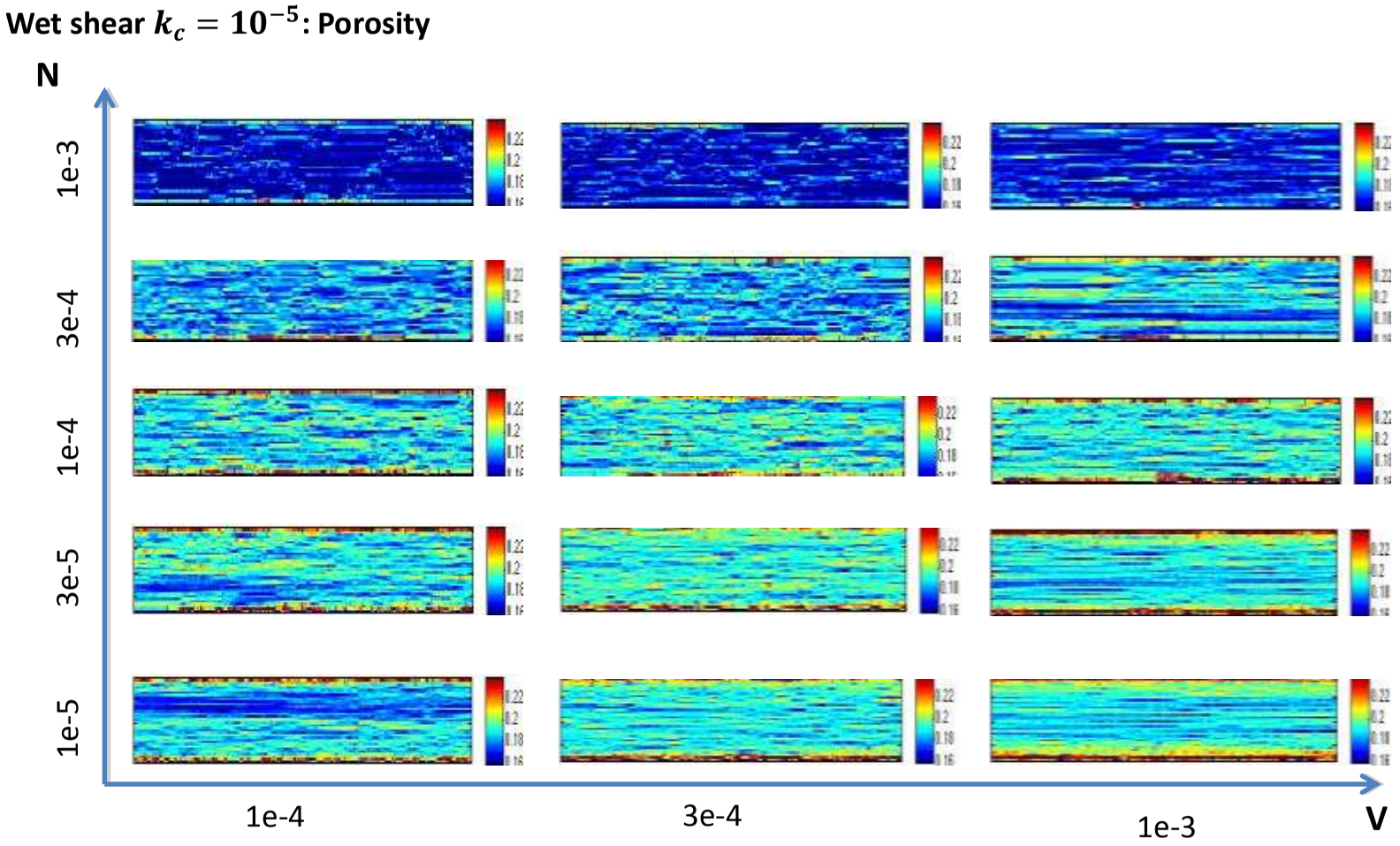

Figure 19 Porosity profiles vs. shear strain for the fluid saturated $k_c = 10^{-5}$ simulations, arranged similarly to Figure 14. There is stronger dilation on the boundaries for increased *V/N*, and there is an overall increase in system dilation with decreasing *N*. We see more horizontal continuity in the internal layers within type (III) systems with increasing *V/N*.

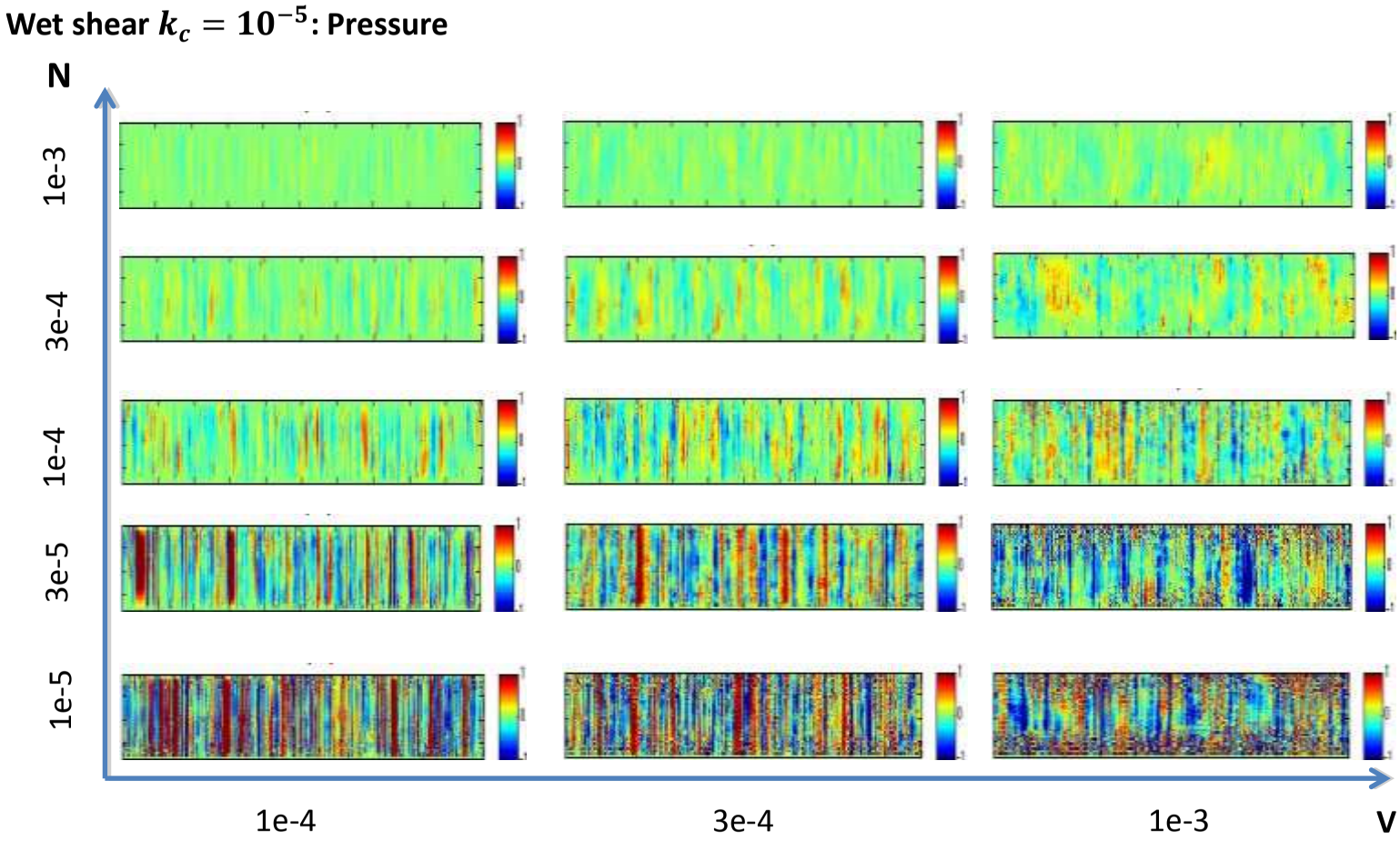

Figure 20 Layer averaged perturbation on pressure calculated and arranged similarly to Figures 11 and 14 for fluid saturated systems with $k_c = 10^{-5}$. Here each of the plots are scaled to N to highlight important changes in pressure. Red values represent $\Delta P \to N$, and blue values are $\Delta P \to -N$. For systems with decreased values of N, we see an increase in ΔP as it becomes easier for the pressures to reach values of N.

We quantify the position of pressure extremes, P_P, the same way as P_L by finding the largest pressure difference between two adjacent cells at an instant in time. Figure 21 shows $P_L \approx P_P$ for low *V/N*, but as *V/N* increases P_L localizes closer to the boundary than P_P. Extreme pressure values are created in the shear bands, but when shear bands form near the boundary the P=0 boundary condition forces the pressure extremes to occur slightly further into the layer.

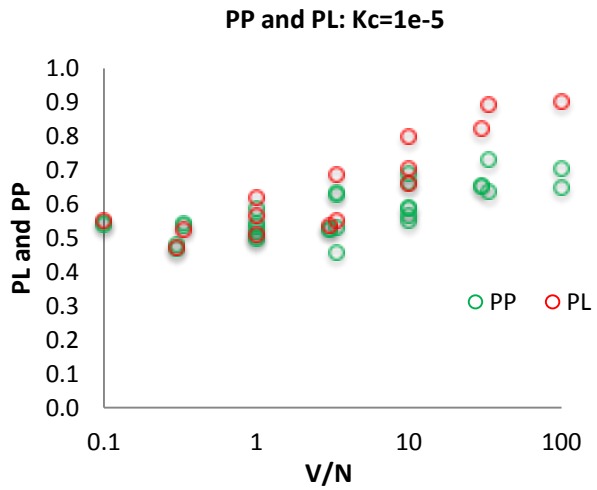

Figure 21 Position of localization, P_L, and pressure, P_P vs. *V/N*. We see that $P_L \approx P_P$ for low *V/N*, but as *V/N* increases and $P_L \to 1$, we see P_P will begin to decrease moving away from the boundary and the shearing bands.

4.2.3 WET SYSTEMS: $k_c = 10^{-6}$

This section describes a set of 15 simulations that were conducted similarly to those of the previous section, except the permeability factor was 10^{-6} (mean permeability ~10^{-15} m^2). We expect to see the localization trends shift in such a way that type (III) shear systems would be present at lower values of *V/N* (Figure 22) than in the dry or higher k_c systems.

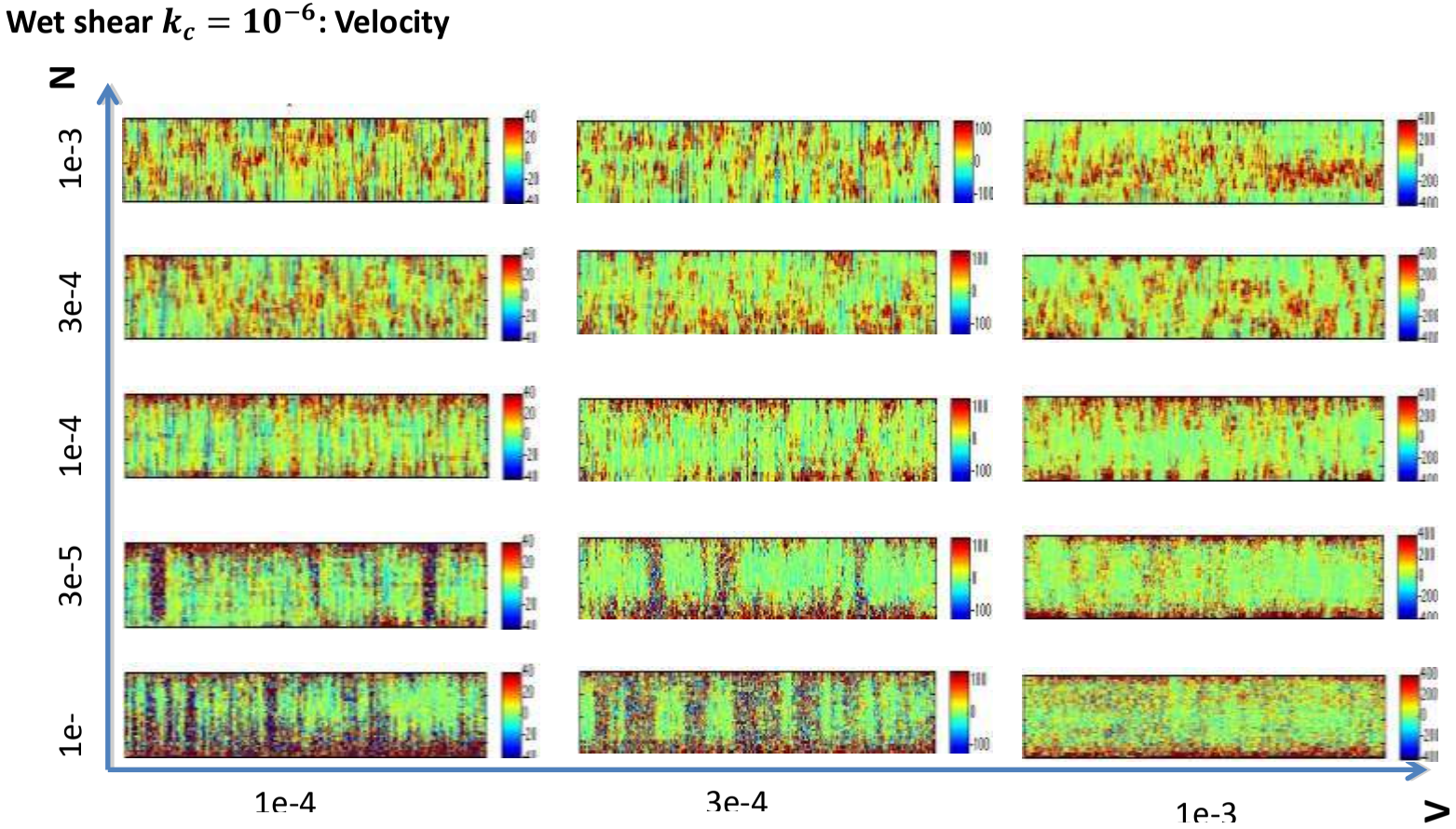

Figure 22 Shear strain rate profiles vs. shear strain for wet simulations with $k_c = 10^{-6}$, arranged similarly to Figure 11. Lower k_c simulations show more boundary localization during type (III) shear for lower *V/N* than the $k_c = 10^{-5}$ systems. The transitional behavior between types (II→III) trend similarly to the $k_c = 10^{-5}$ systems for most *V/N*, except for the systems with low *N* which experience large liquefaction events.

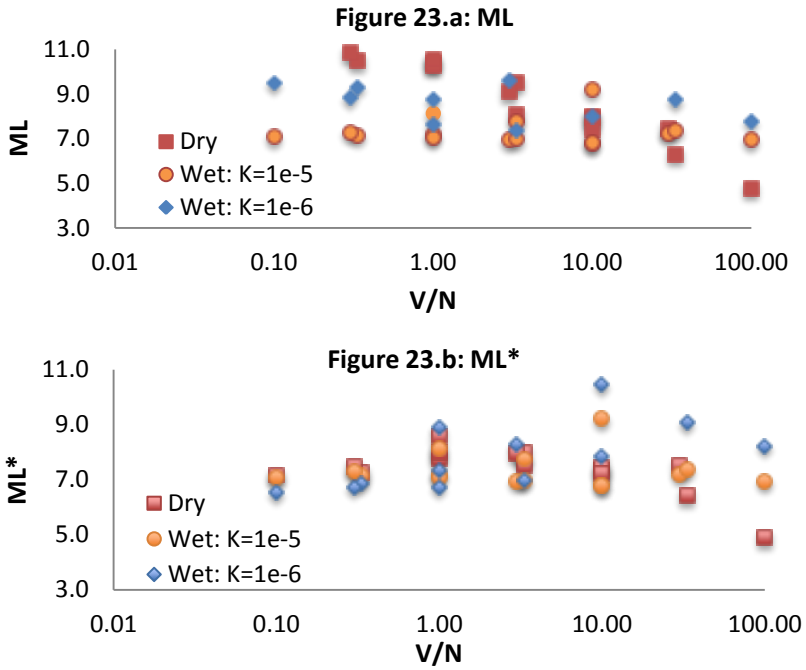

Figure 23 Two measures of the magnitude of localization, (a) M_L and (b) M_L^* vs. *V/N* for both dry and wet simulations ($k_c = 10^{-5}$ and 10^{-6}). (a) More elastic rebound is seen for lower k_c systems (M_L~8-9) for low *V/N*. (b) M_L^* values for both fluid systems remain constant for low *V/N*, but the localization will increase for $k_c = 10^{-6}$ systems with increasing *V/N*.

We do see more shear strain localized to the boundaries for lower *V/N* than the higher k_c systems, but we also see a trend of increasing liquefaction with decreasing *N*, and liquefaction can have a significant effect on localization.

If we remove the data collected during the liquefaction times (during which our localization measures are not valid), we can see a similar trend to the higher k_c experiments. We see higher localization values of M_L for the lower k_c systems for low *V/N*, and a decrease in localization in systems with higher values of *V/N* (Figure 23.a). The values of M_L^* remain fairly constant between the dry and both fluid systems for low *V/N*; however as *V/N* increases, the lower k_c systems will become more localized

(Figure 23.b). We can see this trend in Figure 24, where the lower k_c systems will exhibit type (III) at much lower values of *V/N* than either the dry or higher k_c experiments. This behavior could be due to the number of liquefaction events that are present in the systems at lower *V/N*. A large liquefaction event will generate type (III) shear behavior after the event is over, even at conditions that will more typically have type (II) behavior. These effects will be discussed further in the next section.

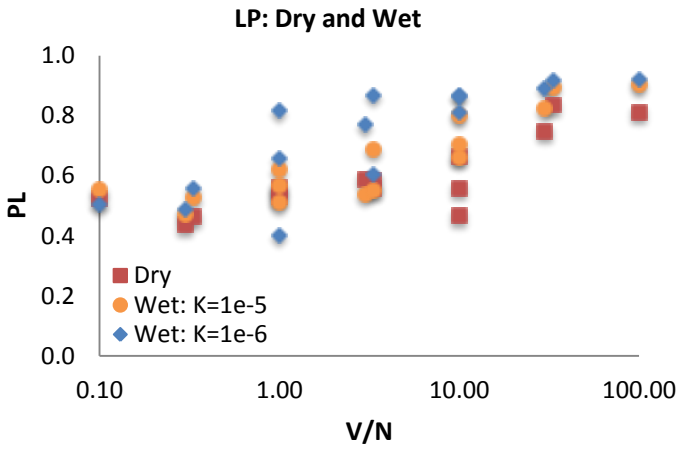

Figure 24 The position of localization, P_L vs. *V/N* for both dry and wet simulations ($k_c = 10^{-5}$ and 10^{-6}). The lower $k_c = 10^{-6}$ systems will show type (III) shear at much lower values of *V/N* than dry or $k_c = 10^{-5}$ systems. These values could be altered by an increase in the duration of liquefaction events at lower *V/N*.

Porosity trends at the lower k_c systems (figure 25) show similar boundary dilation as in the higher k_c systems, along with an increase in internal dilation with decreasing *N*. However, we see that the majority of the dilation within the system is not as internally distributed as it is in the higher k_c system. This can be a result of decreasing

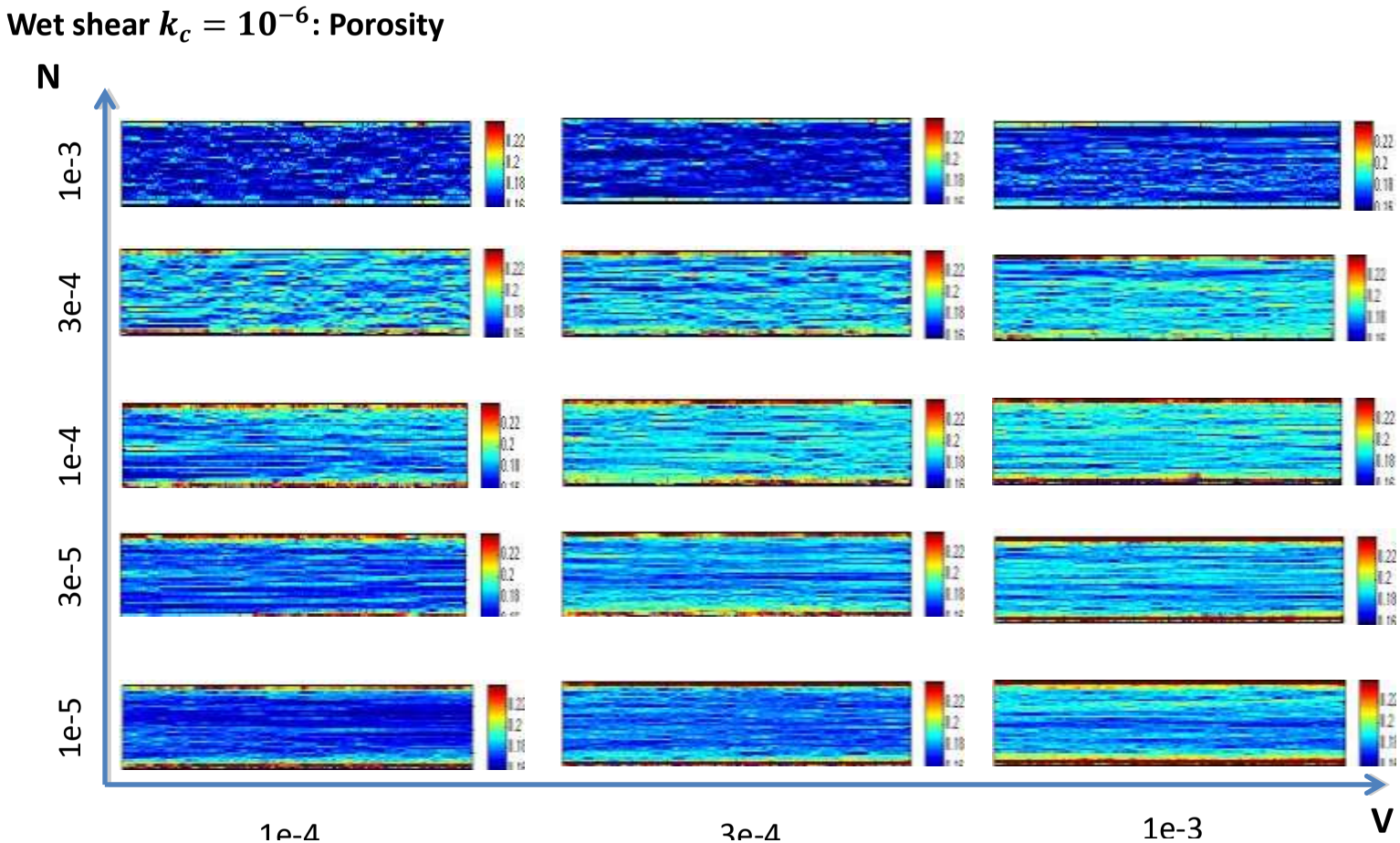

Figure 25. Porosity profiles vs. shear strain for the fluid saturated $k_c = 10^{-6}$ simulations, arranged similarly to Figure 11. The plots show dilation trends similar to the $k_c = 10^{-5}$ systems. We do see an increase in the mean porosity with decreasing *N*, along with a slightly larger porosity along the boundaries. For systems with decreased values of *N*, we see an increase in the thickness and duration of the non-shearing layers within the gouge.

the ability of fluid to flow into the system, which limits compaction and dilation (hence, shear) in the interior of the layer.

We see an increase in pressure for systems with lower values of k_c, which will cause more of the systems to reach liquefaction pressures. We see the same pressure trends with *N* as in the higher k_c systems. Systems with high *V/N* have rapidly alternating extreme pressures, which appear as a block of purple color in Figure 26. This is because we find that the duration of liquefaction events decreases with *V*.

4.3 LIQUIFACTION

We have shown in sections 4.1 and 4.2 that under certain conditions, the gouge layer will liquefy during shear. Figure 27 shows the spatial distribution of pressure variations (top) and the granular stresses (bottom), respectively, at several points in time surrounding a liquefaction event. The areas around force chains are typically lower pressure (dilating as chains are rotated by the shear), while regions between grains are higher pressure (grains are compacting) whether the system is undergoing liquefaction or not. However, during liquefaction events (Figure 27), we see the positive pressures build up around the force chains until they reduce the normal stress on the contacts enough to allow frictional sliding (parts a and b). Once the force chains break apart (part c), the system no longer can transmit shear stress down from the top wall (as shown by the sudden reduction of the apparent friction). Without shear stress, the grains begin to collapse, with porosity decreasing toward the stress-free relaxed value (~0.16). This compaction further increases pressure so that the entire system has P~*N*.

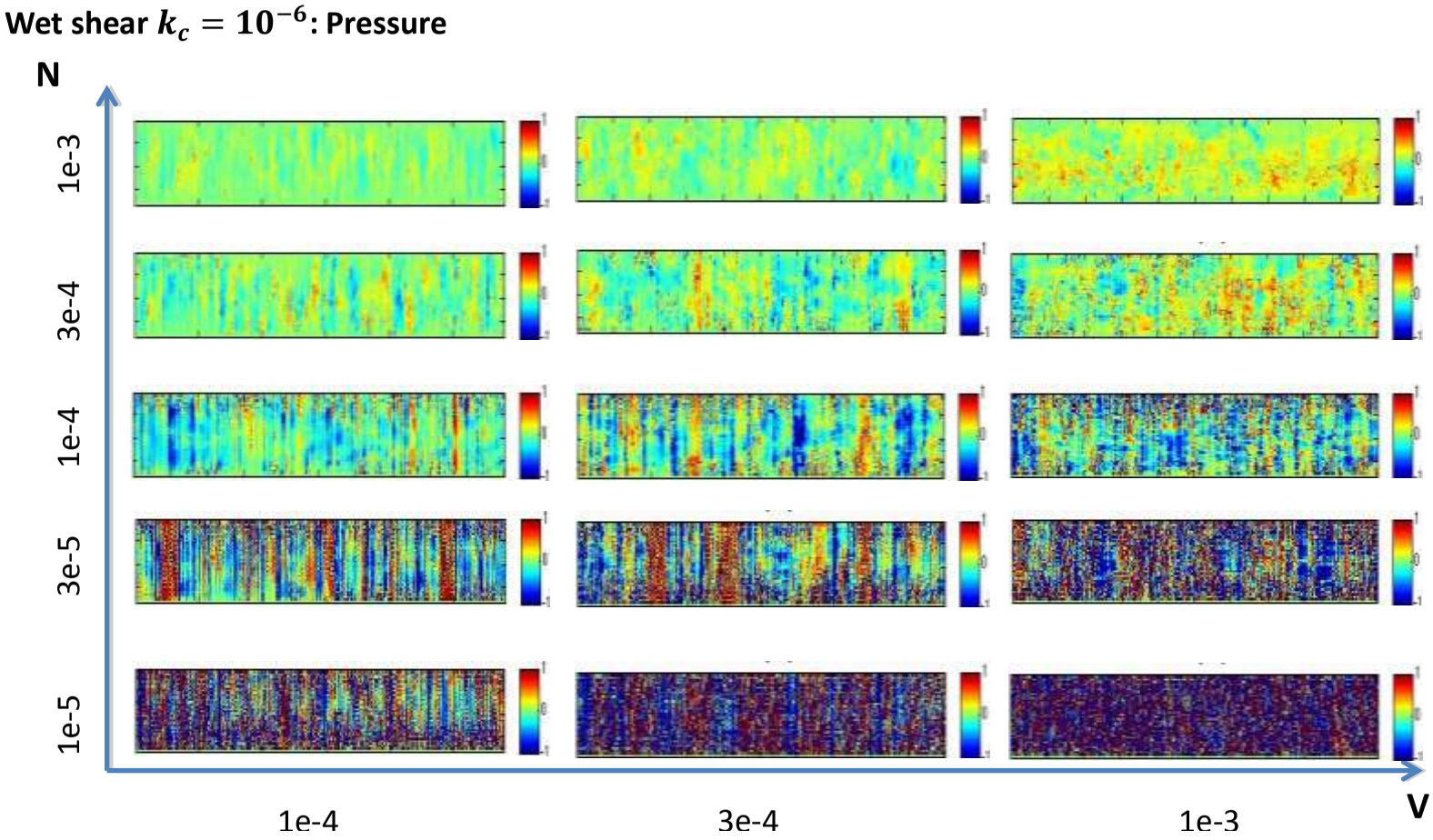

Figure 26. Layer averaged perturbation on pressure calculated and arranged similarly to Figures 11 and 14 for fluid saturated systems with $k_c = 10^{-6}$. We see pressure increases with lower $k_c = 10^{-6}$ systems, which is generating more liquefaction events. The liquefaction events in the low *N* simulations show extreme pressures of $^{+}/_{-}$ *N* that alternate between adjacent grain layers , which shows an increase in liquefaction in systems with increased values of *V*/*N*.

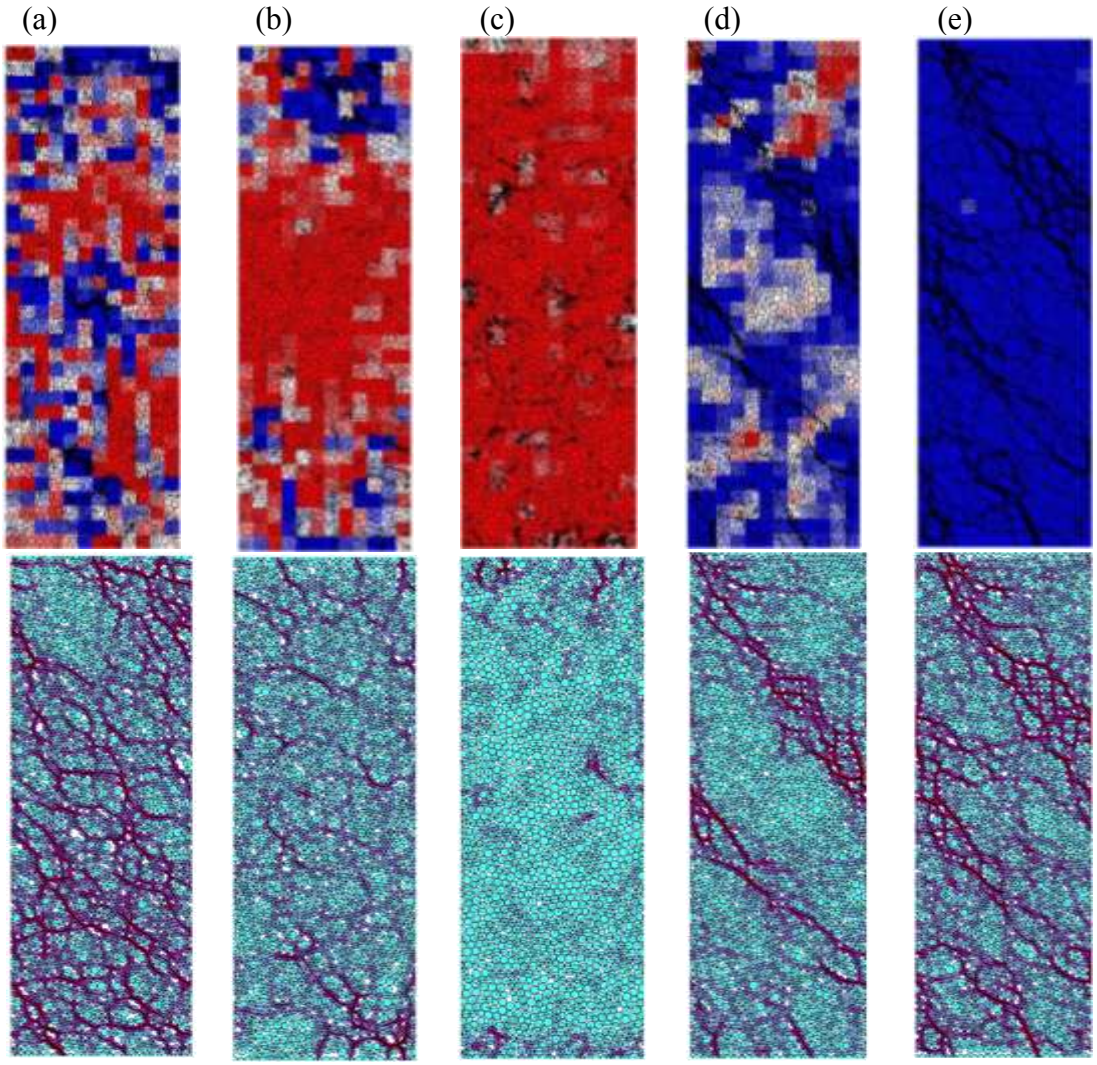

Figure 27 Spatial distribution of pressure perturbations at five different times surrounding a liquefaction event, along with the corresponding force chain images. In this simulation, N=10^{-5}, V=10^{-4}, k_c=10^{-6}. As the system shears, (a) large positive pressures begin to accumulate between the remaining force chains. (b) As pressure gradients increase, the drag forces buckle and destroy force chains in the middle of the system. Without shear stress in the interior, the grains begin to compact driving pressure up. (c) As collapse continues, the pressures in the system approach the normal stress until the fluid can diffuse out of the system. (d) As the grains settle towards a relaxed state, small forces will begin to accumulate until a force chain is created that spans the system. This begins to push the top wall back up, which generates large negative pressures within the system. (e) An interconnected network of contacts reforms around the initial force chain while rapid opening drives large negative pressures.

With no through-going force chains, pressure alone holds up the top wall as it continues to shear. The top wall falls as fast as fluid can be driven out of the system, as shown by the collapse in porosity (Figure 28.c). During this collapse, the confining stress on the top wall is nearly balanced by the drag force of the fluid flowing out of the system. We find that the rate of compaction seen in Figures (28.a-c) is dependent on k_c and not on shear strain rate. The grains will continue to fall towards a relaxed state configuration until a new force chain is created. At this time, the force balance on the top wall is destroyed, and the top wall is forced outward from the gouge causing a large increase in the mean porosity of wall is forced outward from the gouge causing a large increase in the mean porosity of the system, which generates negative pressures within the gouge that act to strengthen the matrix. Figures 28.a-c shows large drops in pressure that correspond to the rapid increase in porosity created by the reformation of force chains after liquefaction events.

Systems with decreased *N*, *V*, and *k* show an increase in the number of liquefaction events. In order for a fluid saturated system of grains to reach liquefaction, the mean pressure deviation within the system must be equal to or exceed the effective normal stress. Decreased k_c restricts the ability for the fluid to flow in/out of the system to equilibrate the internal pressures generated during compaction/dilation events, which causes larger changes in pressure, as diffusion rates are reduced (Figure 28.a-c). For Figure 28.a $k_c = 10^{-5}$ (Figure 28.a), the mean porosity does not deviate far from the mean porosity of the dry systems. However, the pressure plots show that there are times at which the system has pressures equal to or in excess of *N*. The duration of these

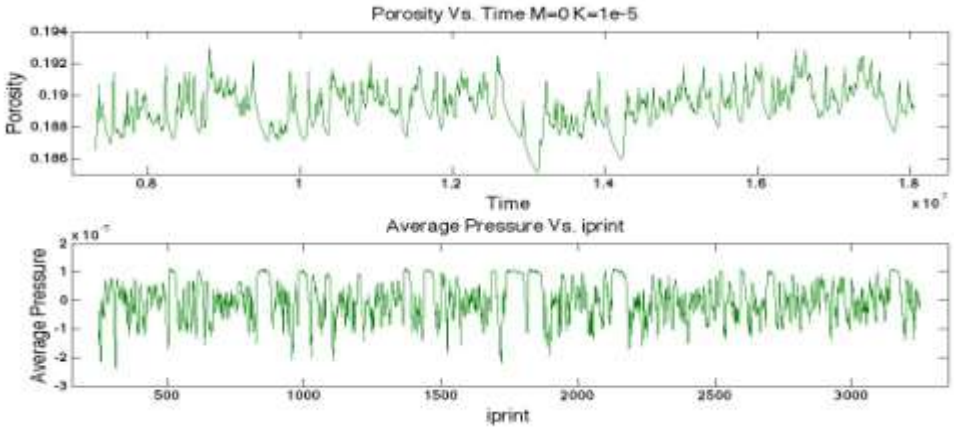

Figure 28.b

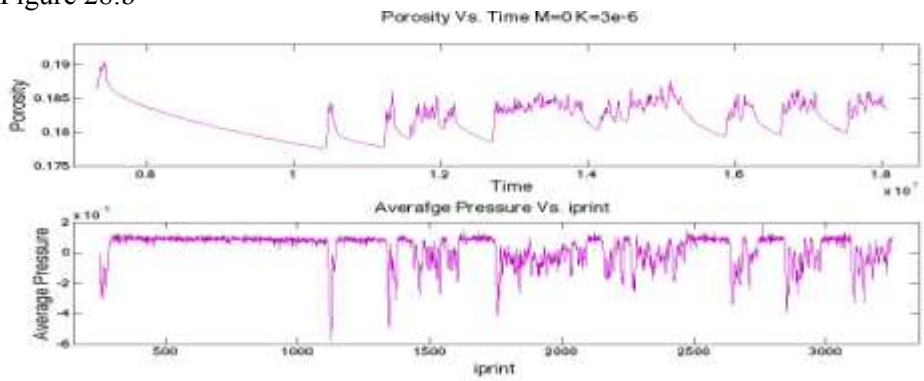

Figure 28.c

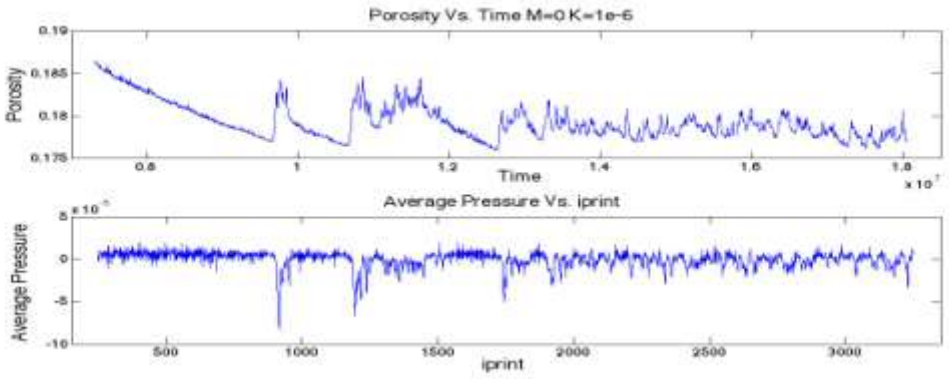

Figure 28 a-c Plots of porosity vs. time and the corresponding pressures for systems with V=10^{-4}, N=10^{-5} and $k_c = (a)10^{-5}, (b)3 * 10^{-6}, (c)10^{-6}$. Each of the plots show both the rate of compaction as a function of k, and the pressures generated during each event. We see large decreases in pressure at the end of each liquefaction event that result in the reformation of force chains that increase porosity and cause the decrease in pressure.

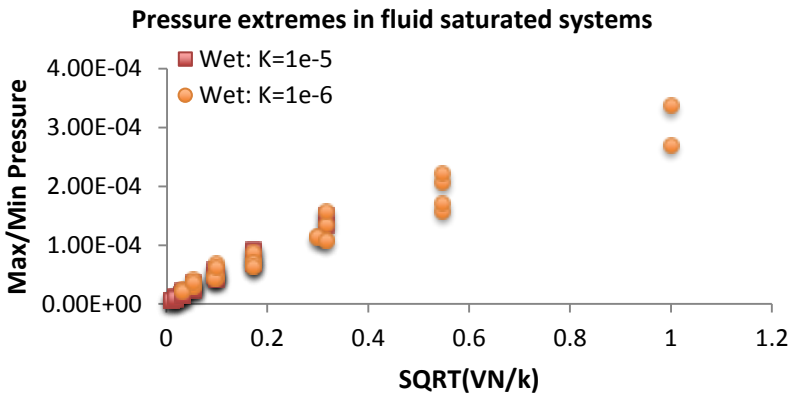

Figure 29 The absolute values of the max/min ΔP across adjacent layers averaged through time. We see here that both the high and low k_c systems increase for $\Delta P \propto \sqrt{\frac{VN}{k}}$.

events increases in systems with lower k_c (Figures 28.b and c).

The shear strain phase diagrams reveal a tendency for boundary localization immediately after a liquefaction event (Figure 22). Lower *V/N* simulations that are undergoing type (II) shear, will exhibit pronounced type (III) shear for strains up to ~4-5 following a liquefaction event, until they slowly begin to transition back to type (II) shear. The very large liquefaction events seen in Figure 22 are present due to the pre-dilated state of the grains before the fluid addition to the system. However, without the large initial events we still see an increase in liquefaction for the systems described above.

We find that the maximum and minimum pressures, averaged over the time are well-described by the relationship

$$\Delta P \propto \sqrt{\frac{VN}{k}}$$

for both high and low k_c systems (Figure 29). Goren et al., 2010 showed that drained systems ($De \sim 1$) shearing along a single plane show should produce pressure variations, $\Delta P \propto \sqrt{V/k}$. The dependence that we see on $\sqrt{N}$ may come from the distribution of shear within shear bands changing with *N*.

Since pressure perturbations that approach *N* have the largest effect on the systems, the frequency and strength of liquefaction events should increase with increasing $\Delta P/N$. Given our observed dependence of ΔP, liquefaction frequency will depend on $\sqrt{\frac{V}{Nk}}$.

5. CONCLUSION

We have shown three types of shear behaviors in our simulations: type I (uniformly distributed shear), type II (localized shear in transient shear bands that form randomly throughout the layer), and type III (localized shear in shear bands at one or both boundaries), as well as transitional states between two different types. Our simulations show the shear behavior of a particular granular system can change depending on the ratio of shear velocity to effective normal stress (*V/N*), and on the importance of fluid flow effects (Figure 30.a). The dry simulations of Shojaaee et al., 2012 show similar results, but they do not see the transitions between all three types of shear behaviors in a single granular system. They found that systems with smooth walls show types II and III behavior, and systems with "very rough" walls will show types II and I.

Wall roughness is controlled by the fixed size and spacing of wall grains. Rough walls will generate more homogeneous shear into the granular material (Figure 30.b), while smooth walls show more shear localization along the boundaries (Figure 30.c). Our model uses semi-rough walls, in between the two cases explored in Shojaaee et al (2012) Shojaaee et al., 2012 find shear trends depend on $V/\sqrt{N}$, through the Inertia Number, *I*. We also find $V/\sqrt{N}$ to be a reasonable predictor of the degree and position of localization in our dry simulations, although not significantly better or worse than *V/N*. However, we find that *V/N* is a better predictor for the fluid saturated systems.

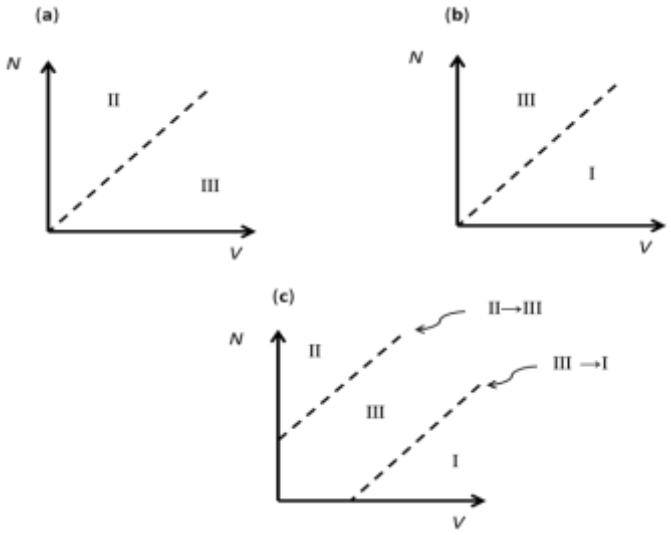

Figure 30 Three idealized phase diagrams giving the transitional behavior for dry systems with different *V/N* seen between types (II, III, I) shear for systems with different wall roughness. (a) smooth wall systems used in Shojaaee et al., 2012, shows a transition between types(II→III) shear, (b) phase diagram for our experiments showing the transition between types(II→III→I) shear for semi-rough boundaries.

Once the systems begin to shear, the system will dilate from a relaxed state to a steady-state porosity. The mean porosity that each system reaches is directly proportional to the effective confining stress, *N*. Dilation of the gouge can only occur through vertical changes in the wall position, which is limited by the magnitude of the confining forces applied to the walls. In a fluid-saturated system, the pressures generated during compaction/dilation will act as a damping force which decreases the variability in porosity (Figure 3), and fluid saturated experiments will shear at a either a slightly larger mean porosity than the dry systems (Figure 6) or, in other cases, a significantly reduced porosity. The first effect is probably due to an increase in fluid flow that results from an increase in permeability with an increased porosity. The second effect occurs in cases with significant liquefaction.

Fluid saturated simulations show more pronounced type (III) boundary localization, as the transition between types (II and III) occurs at lower *V/N* in wet system than the dry systems. However, the magnitude of localization, M_L^*, remains similar for dry and wet for all values of *V/N*<10 (Figure 17.b). Unlike the dry systems, the transition from type III to type I shear is not seen as the fluid systems show P_L~9 toward the boundaries for *V/N*=100 (Figure 18). The increase in P_L is due to the ease of fluid flow in/out of the boundaries relative to flow within the interior of the gouge material.

Systems with lower internal permeability ($k_c = 10^{-6} \approx 10^{-15}\ m^2$) begin to show type (III) shear at lower *V/N* (~1) than the $k_c = 10^{-5}$ experiments, and they are more localized for *V/N*>10. The lower permeability systems generate higher pressures during shear as it is more difficult for the fluid to flow within the gouge layer. This accentuates the ease of diffusion across the boundaries, which is shown by the increase in P_L for lower *V/N*. The restricted fluid flow also makes shearing on multiple layers more difficult as pressures around the shear bands will act to confine the pressures being generated during shear. Therefore, we see more localization (M_L^*~9) for lower *V/N* than the higher k_c experiments.

For gouge zones with moderate to low permeability and low *N* (shallow faults or faults with high background *P*), slip will tend to be on the edge of the gouge, not in the interior; this will tend to grind up the adjacent wall rock and grow the thickness of the gouge with every event. As the fault continues to shear along the boundaries of the gouge layer, microfractures will form along the boundary that increases the permeability

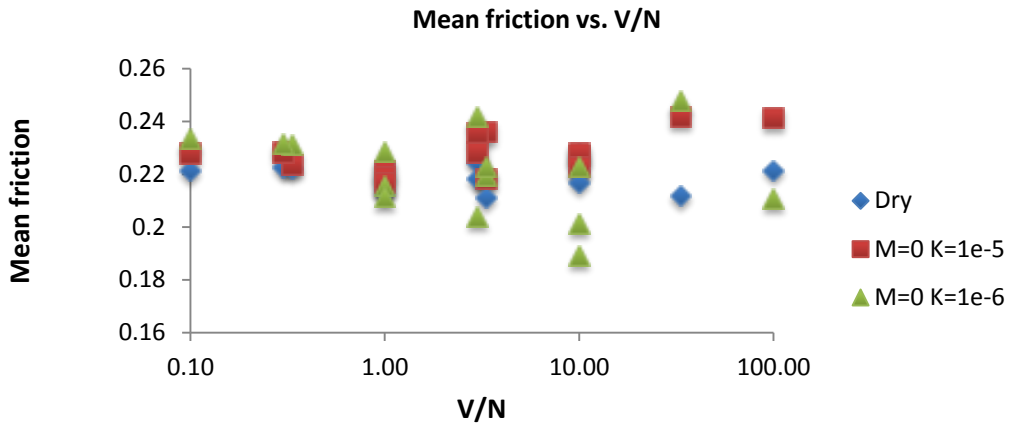

Figure 31 Mean friction vs. *V/N* for all dry and wet systems. We see that fluid has a minimal effect on the mean friction of the systems for low *V/N*. Here, either the velocities are too slow to generated high pressures, or *N* is large and it is harder for ΔP to reach values of *N*. Alternately, at high *V/N* we see a trend of type (III) shear as the fluid begins to increase the mean friction and drive localization to the boundaries, with the exception of low k_c systems with large liquefaction events. For high *V/N* the systems have higher *V*, which generated higher ΔP, and at low *N* it is easy for the pressures to reach and exceed *N*.

of the wall rock (Mitchell and Faulkner, 2012). It is well known that mature fault materials can act as fluid flow barriers as they generally have low permeability, however this permeability can be significantly increased within the damage zone of faults due to the interconnectivity of fractures (Caine et al., 1996, Faulkner et al., 2010). The increase in permeability through these microfractures will continue to perpetuate type (III) shear along the boundaries, which will cause continued deformation of the wall rock. Faults that shear within the gouge layer (type II), will continuously deform the grains within the shear bands, which causes a decrease in the internal permeability of the gouge layer. As the fluid flow within the gouge decreases, the shearing bands will begin to

Table 3. The percent of time that each $k_c = 10^{-6}$ system is liquefied for strain of 20. These values are calculated for all times throughout the experiment that has a mean grain contact less than 2.5. For systems with lower $k_c = 10^{-6}$, we see an increase in liquefaction times for systems with decreased *V* and *N*, and a large increase in liquefaction time in relation to the higher $k_c = 10^{-5}$ systems (Table 4).

N	V=10^{-3}	V=3×10^{-4}	V=10^{-4}
10^{-3}	0 %	0%	0%
3×10^{-4}	0%	0%	0%
10^{-4}	0%	0%	0%
3×10^{-5}	6.86%	8.60%	3.40%
10^{-5}	17.17%	46.90%	87.45%

transition to the boundaries as it becomes easier for fluid to flow in or out of the boundaries transitioning to type (III) shear localization. This transition will drive the cycle discussed above, which causes deformation along the boundaries of the wall rock, instead of further deforming the granular matrix. Transitioning from type (II) into type (III) shear also shows an overall increase in the mean frictional forces (fault strength) seen between grains in fluid saturated systems, with the exception of simulations with large liquefaction events (Figure 31). We see that fluid has a minimal effect on the mean friction of the systems for low V/N. Here, either the velocities are too slow to generated high pressures, or N is large and it is harder for ΔP to reach values of *N*. Alternately, at high V/N we see a trend of type (III) shear as the fluid begins to increase the mean friction and drive localization to the boundaries, with the exception of low k_c systems with large liquefaction events. For high *V*/*N* the systems have higher *V*, which generated higher ΔP, and at low *N* it is easy for the pressures to reach and exceed *N*.

We see an increase in the percentage of time a system is liquefied in simulations

with lower k_c and lower *N* (Table 3). There are small liquefaction events in the $k_c = 10^{-5}$ simulations (Table 4), but the higher permeability will diffuse ΔP out of the system faster, limiting the duration of liquefaction and increasing the overall stability of the gouge layer. This confirms the results of Goren et al. (2010), that liquefaction can occur even in drained fault gouge, as long as the De$\geq$ 1. Systems with large amounts of liquefaction events (high *V*/*N* and low k_c) show large decreases in mean friction to values of ~0.19-0.2, which will weaken faults during shear (Figure 31). The reduced friction seen here is similar to observed behavior in some faults during major earthquakes (C.H. Scholz 1996), which is attributed to thermal pressurization of the pore fluids. This work demonstrates a different potential mechanism to dynamically create low friction during high velocity shear, independent of thermal effects.

Table 4. The percent of time that each $k_c = 10^{-5}$ system is liquefied for strain of 20. These values are calculated for all times throughout the experiment that has a mean grain contact less than 2.5. There is an increase in the time each simulation is liquefied for systems with decreased *N* and increased *V*.

N	*V*=10^{-3}	*V*=3×10^{-4}	*V*=10^{-4}
10^{-3}	0%	0%	0%
3×10^{-4}	0%	0%	0%
10^{-4}	0%	0%	0%
3×10^{-5}	0.70%	0.20%	0%
10^{-5}	7.96%	5.10%	1.15%

REFERENCES

Aharonov, E and D.W. Sparks. 1999. “Rigidity phase transition in granular packings.” *Physical Review* 60: 6890-6896.

Aharonov E. and D.W. Sparks. 2002. “Shear profiles and localization in simulations of granular materials.” *Phys. Rev*. 65(5). doi: 10.1103/PhysRevE.65.051302.

Aharonov, E. and D.W. Sparks. 2004. “Stick-slip motion in simulated granular layers.” *Journal of Geophysical Research-Solid Earth* 109, B09306.

Antonellini, M.A., D.D. Pollard. 1994. “Distinct element modeling of deformation bands in sandstone.” *Journal of Structural Geology* 17, 8:1165-1182.

Ausilio, E., A. Costanzo, F. Silvestri, and G. Tropeano. 2008. “Prediction of seismic slope displacements by dynamic stick-slip analysis.” *American Institute of Physics* 978-0-7354-0542-4:475-484.

Beeler, N.M., T.E. Tullis, M.L. Blanpied, and J.D. Weeks. 1996. “Frictional behavior of large displacement experimental faults.” *Journal of Geophysical Research-Solid Earth* 101,8697-8715.

Byerlee, J. 1990. “Friction, overpressure and fault normal compression.” *Geophys. Res. Lett.* 17:2109-2112. doi:10.1029/GL017i012p02109.

Cain, J.S., J.P. Evans, C.B. Forster. 1996. “Fault zone architecture and permeability structure.” *Geology* 24:1025-1028.

Chester, F. 1982. “Mechanical testing of fault zone materials.” *American Geophysical Union* 63, 45: 1108.

Chester, F.M., and J.S. Chester. 2000. “Stress and deformation along wavy frictional faults.” *J.Geophys. Res.* 105, 23:421-23. doi: 10.1029/2000JB900241.

Chester, F.M. and J.M. Logan. 1987. “Composite planar fabric of gouge from the punchbowl fault, California”. *Journal of Structural Geology* 9:621-634.

Ciamarra, M.P., F. Dalton, L. de Arcangelis, C. Godano, E. Lippiello, A. Petri. 2012. “The role of interstitial impurities in the frictional instability of seismic fault models.” *Tribol Lett* 48:89-94. doi:10.1007/s11249-012-2254-3.

Cundall, P. and O.D.L. Strack. 1979 “Discrete numerical-model for granular assemblies.” *Geotechnique* 29, 1:47-65.

Ebrahimian, B., A. Noorzad, and M.I. Alsaleh. 2011. “Effects of periodic fluctuations of micro-polar boundary conditions on shear localizations in granular soil-structure interaction.” *International Journal for Numerical and Analytical Methods in Geomechanics* 36:855-880. doi:10.1002/nag.1031.

El Shamy, U., and M. Zeghal. 2007. “A micro-mechanical investigation of the dynamic response and liquefaction of saturated granular soils.” *Soil Dyn. Earthquake Eng.* 27 8:712–729. doi:10.1016/j.soildyn.2006.12.010.

Faulkner, D.R., C.A.L. Jackson, R.J. Lunn, R.W. Schlische, Z.K. Shipton, C.A.J. Wibberley, M.O. Withjack. 2010. “A review of recent developments concerning the structure, mechanics and fluid flow properties of fault zones.” *Journal of Structural Geology* 32:1557-1575.

Goren, L., E. Aharonov, D.W. Sparks, and R. Toussaint. 2010 “Pore pressure evolution in deforming granular material: A general formulation and the infinitely stiff approximation.” *Journal of Geophysical Research-Solid Earth* 115.

Goren, L., E. Aharonov, D.W. Sparks, and R. Toussaint. 2011 “The mechanical coupling of fluid-filled granular material under shear.” *Pure and Applied Geophysics* 168, 2289-2323. doi:10.1007/s00024-011-0320-4.

Graziani, A., C. Rossini, T. Rotonda. 2012. “Characterization and DEM Modeling of shear zones at a large dam foundation.” *International Journal Of Geomechanics* doi: 10.1061/(ASCE)GM.1943-5622.0000220.

Guo, P. 2012. “Critical length of force chains and shear band thickness in dense granular materials.” *Acta Geotechnica* 7:41–55. doi: 10.1007/s11440-011-0154-3.

Hadizadeh, J., Sehhati, R., Tullis, T. 2010. “Porosity and particle shape changes leading to shear localization in small-displacement faults.” *Journal of Structural Geology* 32:1712e1720. doi:10.1016/j.jsg.2010.09.010.

Healy, D., R.R. Jones, and R.E. Holdsworth. 2006. “Three-dimensional brittle shear by tensile crack interaction.” *Nature* 439:64-67. doi: 10.1038/nature04346.

Iverson, R. 1993. “Differential equations governing slip-induced pore-pressure fluctuations in a water-saturated granular medium.” *Mathematical Geology* 25, 8. doi:0882-8121/93/l100-1027507.00/1.

Jian-Fei Chen. J.A., J.M. Rotter, J.Y. Ooi. 2010. "Assessment of rolling resistance models in discrete element simulations." *Powder Technology* 206:269–282. doi:10.1016/j.powtec.2010.09.030.

Jiang, M.J., Yan, H.B., Zhu, H.H., Utili, S. 2011. "Modeling shear behavior and strain localization in cemented sands by two-dimensional distinct element method analyses." *Computers and Geotechnics* 38:14–29. doi:10.1016/j.compgeo.2010.09.001.

Jónsson, S., P. Segall, R. Pedersen, G. Björnsson. 2003. "Post-earthquake ground movements correlated to pore-pressure transients." *Nature* 424:179-183.

Kock, I. and K. Huhn. 2007. "Influence of particle shape on the frictional strength of sediments — A numerical case study." *Sedimentary Geology* 196:217–233. doi:10.1016/j.sedgeo.2006.07.011.

Lockner, D.A. 1998. "A generalized law for brittle deformation of Westerly granite." *J. Geophys. Res.* 103:5107-5123. doi:10.1029/97JB03211.

Mair, K. and S. Abe. 2011. "Breaking up: Comminution mechanisms in sheared simulated fault gouge." *Pure Appl. Geophys.* 168:2277–2288. doi:10.1007/s00024-011-0266-6.

Mair, K. and J.F. Hazzard. 2007. "Nature of stress accommodation in sheared granular material: Insights from 3D numerical modeling." *Earth and Planetary Science Letters* 259:469-485. doi:10.1016/j.epsl.2007.05.006

Makedonska, N., D.W. Sparks, E. Aharonov, L.Goren. 2011. "Friction versus dilation revisited: Insights from theoretical and numerical models." *Journal of Geophysical Research. Solid Earth* 116.9. doi:http://dx.doi.org/10.1029/2010JB008139.

Marone, C., C.B. Raleigh, and C.H. Scholz. 1990. "Frictional behavior and constitutive modeling of simulated fault gouge." *Journal of Geophysical Research-Solid Earth and Planets* 95:7007-7025.

McNamara, S., E.G. Flekkøy, and K.J. Maløy. 2000. "Grains and gas flow: Molecular dynamics with hydrodynamic interactions." *Phys. Rev.* 61(4):4054 – 4059.

Mitchell T.M. and D.R. Faulkner. 2008 "Experimental measurements of permeability evolution during triaxial compression of initially intact crystalline rocks and implications for fluid flow in fault zones." *J. Geophys. Res*. 113, B11412. doi:10.1029/2008jb005588.

Miller, S. A. and A. Nur. 2000. "Permeability as a toggle switch in fluid controlled crustal processes". *Earth Planet. Sci. Lett*. 183:133–146.

Mitchell T.M. and D.R. Faulkner. 2012. "Towards quantifying the matrix permeability of fault damage zones in low porosity rocks." *Earth and Planetary Science Letters* 339-340:24-31.

Morgan, J.K. and M.S. Boettcher. 1999. "Numerical simulations of granular shear zones using the distinct element method - 1. Shear zone kinematics and the micromechanics of localization." *Journal Of Geophysical Research-solid Earth* 104(B2):2703-2719.

Okada, Y., H. Ochiai. 2007. “Coupling pore-water pressure with distinct element method and steady state strengths in numerical triaxial compression tests under undrained conditions.” *Landslides* 4:357–369. doi:10.1007/s10346-007-0092-1.

Place, D. and P. Mora. 1999. “The lattice solid model to simulate the physics of rocks and earthquakes: Incorporation of friction.” *Journal of Computational Physics* 150, 2:332-372.

Robin, P.-Y. F. 1973. “Note on effective pressure.” *Journal of Geophysical Research* 78(14):2434–2437.

Rozhko, A. Y., Y. Y. Podladchikov, and F. Renard. 2007. “Failure patterns caused by localized rise in pore-fluid overpressure and effective strength of rocks.” *Geophys. Res. Lett.* 34, L22304, doi:10.1029/2007GL031696.

Samuelson, J., D. Elsworth, C. Marone. 2009. “Shear-induced dilatancy of fluid-saturated faults: Experiment and theory.” *Journal of Geophysical Research* 114, B12404. doi:10.1029/2008JB006273.

Scholz, C.H. 1996. “Faults without friction?” *Nature* 381:556-557. doi:10.1038/381556a0.

Scholz, C.H., L.R. Sykes, and Y.P. Aggarwal. 1973. “Earthquake prediction - physical basis.” *Science* 181(4102):803–810.

Segall, P. and J.R. Rice. 1995. “Dilatancy, compaction, and slip instability of fluid-infiltrated fault.” *Journal of Geophysical Research* 100(B11):22:155–22:171.

Segall, P., A.M. Rubin, A.M. Bradley, and J.R. Rice. 2010. “Dilatant strengthening as a mechanism for slow slip events.” *Journal of Geophysical Research* 115, B12305. doi:10.1029/2010JB007449.

Sheldon, H.A., A.C. Barncoat, A. Ord. 2006. “Numerical modeling of fault and fluid flow in porous rocks: An approach based on critical state soil mechanics.” *Journal of Structural Geology* 28:1468-1482. doi:10.1016/j.jsg.2006.03.039.

Shojaaee, Z., J.N. Roux, F. Chevoir, D.E. Wolf. 2012. “Shear flow of dense materials near smooth walls. I. Shear localization and constitutive laws in the boundary region.” *Physical Review* 86, 011301. doi:10.1103/PhysRevE.86.011301.

Sibson, R.H. 1990. “Conditions for fault-valve behavior.” *Deformation Mechanisms Rheology and Tectonics* edited by R.J. Knipe and E.H. Rutter, Geol. Soc. London Spec. Publ., 54:15-28.

Sleep, N. H., and M. L. Blanpied. 1992. “Creep, compaction and the weak rheology of major faults” *Nature* 359(6397), 687–692, doi:10.1038/ 359687a0.

Tejchman, J. 2006. “Effect of fluctuation of current void ratio on the shear zone formation in granular bodies within micro-polar hypoplasticity.” *Computers and Geotechnics* 33:29–46.

Tejchman, J. and W. Wu. 2010. “Boundary effects on behavior of granular material during plane strain compression.” *European Journal of Mechanics A/Solids* 29:18-27. doi:10.1016/j.euromechsol.2009.07.004.

Terzaghi, K. 1943. “Theoretical soil mechanics.” John Wiley, New York.

Wong, T. and P. Baud. 2012. “The brittle-ductile transition in porous rock: A review.” *Journal of Structural Geology* 44:25e53.

Yamashita, T. 1999. “Pore creation due to fault slip in a fluid-permeated fault zone and its effect on seismicity: Generation mechanism of earthquake swarm.” *Pure Appl. Geophys.* 155: 625–647. doi:0033–4553:99:040625–23 1.50_0.20:0.